Thesis for The Degree of Licentiate of Engineering

Numerical Investigation of Scale Effects on Cavitation and Underwater Radiated Noise

Qais Shehadeh Khraisat

Department of Mechanics and Maritime Sciences
Chalmers University of Technology
Gothenburg, Sweden, 2024

Numerical Investigation of Scale Effects on Cavitation and Underwater Radiated Noise

Qais Shehadeh Khraisat

Department of Mechanics and Maritime Sciences
Division of Marine Technology
Chalmers University of Technology
SE-412 96 Göteborg,
Sweden
Phone: +46(0)31 772 1000

Chalmers Reproservice
Gothenburg, Sweden 2024.

Numerical Investigation of Scale Effects on Cavitation and Underwater Radiated Noise

Qais Shehadeh Khraisat

Department of Mechanics and Maritime Sciences
Division of Marine Technology
Chalmers University of Technology

Abstract

Recent research efforts to reduce shipping noise emissions have been motivated by the growing awareness of its adverse effect on marine life. At this moment, there is a need for reliable noise assessment methods to support in designing more silent vessels. While sea trial measurements and model scale tests provide valuable data, they cannot be used during the early stages of ship design. Numerical methods, on the other hand, offer the tools for the assessment of noise emissions during these early stages. However, there is currently no well-established, consistent, and reliable approach for the prediction methods. In addition, the lack of research on scale effects on cavitation limits the ability to make informed design decisions.

In this research work, the objectives focus on the assessment of scale effects on cavitation and the development of reliable tools for predicting underwater radiated noise from ships. Studied cases include a cavitating hydrofoil and a propeller operating in-behind condition. Results show that scale effects are more significant for the propeller case due to the interaction with the wakefield. At full scale, cavitation is less pronounced, which leads to significant differences in both pressure pulse levels and underwater radiated noise. In addition to scale effects, the impact of the domain/tunnel size on cavitation is investigated. Results indicate that blockage influences the wakefield upstream of the propeller, leading to less cavitation when using a larger computational domain.

For the noise assessment, it is demonstrated that using the Ffowcs Williams–Hawkings acoustic analogy for hydroacoustic applications can produce inconsistent results. An alternative noise prediction methodology is proposed which models cavitation as a monopole source. Results are compared with sea trial measurements and model scale tests. While good agreement is obtained for pressure pulses, discrepancies occur for the noise level predictions. At low frequencies, sea trial measurements are dominated by engine noise, a source not accounted for in the numerical predictions. Better agreement is obtained when compared with model tests, but the numerical predictions still significantly underpredict the broadband noise levels. The results highlight challenges in obtaining reliable noise predictions and the need for more research in this area.

Keywords Cavitation, Underwater radiated noise, Scale effects, Pressure pulse levels, CFD

Acknowledgement

First, I would like to thank my supervisor Professor Rickard Bensow for his support throughout my research journey. His guidance, experience, and patience have been instrumental in shaping this work and my educational path. I am also grateful to my co-supervisor Martin Persson for providing his valuable experience and continuous support.

Thanks to all my colleagues within the Marine Technology division who have created a supportive, friendly, and most importantly an enjoyable work environment. I look forward to more discussions on CFD, food, and the many other nonsensical topics.

Finally, I would like to extend very special thanks to my parents Shehadeh and Fatima, my wife Dana, my brothers and sister for always being there for me every step of the way. I hope to continue growing and becoming a better version of myself for you.

List of Appended Publications

Two papers are appended with this thesis:

- **Paper I**: Khraisat, Q.S., Persson, M., and Bensow R. Scale effect on cavitation: A study on cavitating hydrofoil and propeller operating in-behind condition. (*To be submitted*)
- **Paper II**: Khraisat, Q.S., Persson, M., and Bensow R. Cavitation Underwater Radiated Noise Methodology Applied to a Propeller Operating in-behind Condition. (*To be submitted*)

Other Publications:

- Khraisat, Q. S., Persson, M., and Bensow, R. E. (2024). Prediction of cavitation and underwater radiated noise for a propeller operating in-behind condition. In Proceedings of the Cavitation Symposium (Cav 2024).
- Khraisat, Q. S. A., Persson, M., Vikström, M., and Bensow R. (2024). Scale effects on cavitation on a hydrofoil. In Proceedings of the Eighth International Symposium on Marine Propulsors (smp'24, pp. 335–344).
- Khraisat, Q., Lopes, R.., Persson, M., and Bensow R. (2023). Assessing scale effects on a propeller in uniform inflow condition. In the proceedings of the 25th Numerical Towing Tank Symposium (NuTTS 2023).

Contents

Part I

Summary of Work

Chapter 1

Introduction

1.1 The Problem of Underwater Radiated Noise from Shipping

There is a common misconception that deep seas and oceans are quiet environments, which has been spread by the media. The titles chosen by Jacques Cousteau and Louis Malle for their 1956 documentary "The Silent World", or more recently Anthony Koslow's book "The Silent Deep", may lead one to think so. However, oceans and seas are no longer silent due to many human activities including shipping. Underwater Radiated Noise (URN), particularly from commercial vessels, has recently become a global environmental concern.

Historically, the interest in URN has been mainly limited to military applications, such as warships and submarines. With the growing environmental awareness of the impact of noise on marine life, research activities have recently extended to include commercial vessels. Studies show that the hearing range of many marine mammals overlaps with the noise emissions from ships as shown in Figure 1.1. Furthermore, the increased noise levels from shipping compared with ambient noise shown in Figure 1.2 indicates to a rise of more than 30 dB in frequencies between 10 to 100 Hz.

Other studies report that noise emissions from the shipping industry are continuously increasing each year due to growing activities and economic growth. On average, underwater noise level have increased by 3.3 dB per decade [3], and more recently is predicted to double every 11.5 years [4]. Given these trends and the overlap between shipping noise and the hearing ranges of marine animals, concerns have been raised about the environmental consequences. Evidence indicating to the negative impact of shipping noise is published in [5], showing a blue whale's movement pattern trapped by the lanes of passing vessels. In addition, the studies summarized by Duarte et al. [6] reveal that anthropogenic noise, including shipping noise, interferes with the auditory environment and referred to this effect as "masking". The masking effect interferes with their communication, navigation, finding prey, and avoiding predators.

To protect the marine life, URN has been recognized as an environmental hazard by the International Maritime Organization (IMO), which motivated efforts to propose recommendations and guidelines to mitigate its levels [7]. A revised version of these guidelines was released in 2023 providing updated

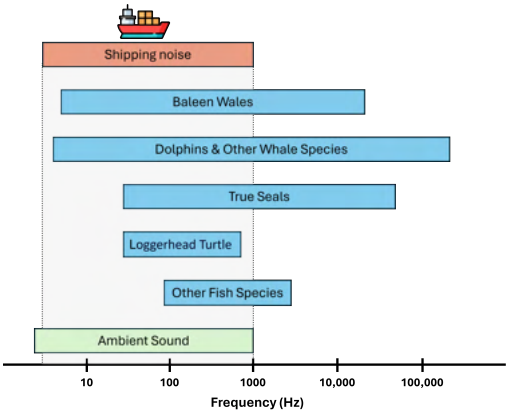

Figure 1.1: Hearing frequency ranges of various species along with the main energy frequencies from shipping and ambient sources. Data and figure adopted from [1]

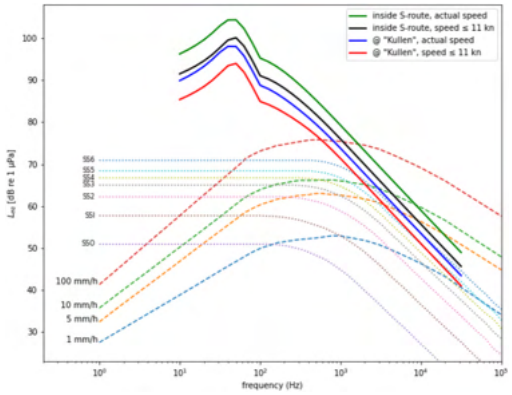

Figure 1.2: Ambient noise (dashed lines) and average shipping noise spectra (solid lines) [2].

recommendations related to ship design, onboard machinery, maintenance, and operational decisions [8]. Regarding operational decisions, [2] demonstrated that mandating vessel speeds to 11 knots can lower levels by an average of 4.4 ± 2 dB. However, the implications on efficiency, other pollutants, and economics are not yet fully understood. Furthermore, such guidelines are not mandatory, and the task of reducing noise emissions from ships remains underdeveloped. This is largely due to current research challenges, including reliable assessment of radiated levels and effective mitigation techniques.

1.2 Ships as a Source of Underwater Radiated Noise

As ships travel through water, they continuously generate noise from different sources which propagate over long distances. Here, it is important to distinguish between sound and noise. Sound is a broad term and referring to vibrations traveling through a medium, while noise is more specific and describes unpleasant or unwanted sound that causes annoyance. As shown in Figure 1.3, the sources can be generally classified into three main categories: machinery noise, hydrodynamic noise, and propeller noise [9].

Machinery noise refers to the sound produced by the propulsion system, including the engine and other auxiliary equipment such as generators and pumps. This type of noise is mainly caused by the mechanical vibrations from moving parts. For instance, the reciprocating motion of engine cylinders and the combustion process can induce vibrations in the hull, which are then transmitted into the surrounding water. In applications of silent vessels, structural noise from auxiliary machinery can become the dominant source [10].

Hydrodynamic noise is generated by flow irregularities and fluctuations caused by turbulent flow around the hull and appendages. Examples include

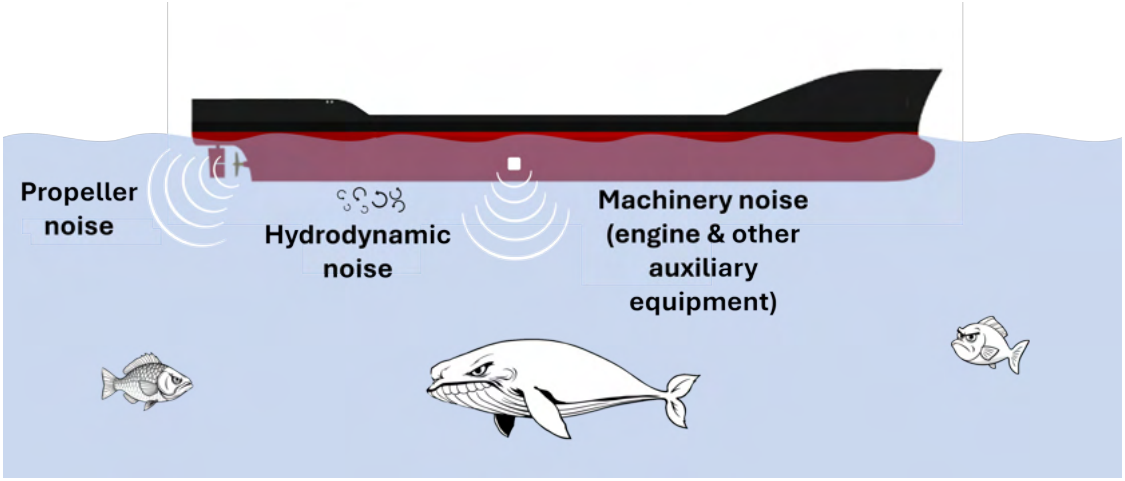

Figure 1.3: Sources of noise from ships.

flow separation and vortex shedding. These noise mechanisms can become more significant at high speeds or high Reynolds numbers. In addition, the fluctuations will induce mechanical vibrations to the structure which further contribute to the total underwater radiated noise signature.

While **propeller noise** can be classified as part of machinery noise, the underlying noise mechanisms are significantly more complex. Unlike other machinery components, the propeller surfaces are in direct contact with the surrounding water, making them more efficient at radiating noise. Also, the noise generation mechanisms from a propeller are dependent on its operation. In non-cavitating conditions, the noise mechanisms are primarily associated with two components. The first is related to disturbances caused by water displacement due to blade rotation and thickness. The second mechanism is associated with pressure fluctuations on the blade surfaces due to unsteady loading, including contributions from the leading and trailing edge noise. However, efficient propellers typically operate in a cavitating regime, which introduces two additional noise mechanisms. One is the dynamic behavior of the cavity structures, which is driven by the inhomogeneous wakefield upstream of the propeller. The other is the noise produced by the rapid collapse of the vapor bubbles, which generates high energy and strong pressure fluctuations that radiate in the surrounding water.

In this context, cavitation refers to the formation of vapor bubbles in liquid water when the local static pressure drops below the vapor pressure. Several types of cavitation may appear on marine propellers as shown in Figure 1.4. The most common are sheet and tip vortex cavitation. Sheet cavitation typically develops when the pressure distribution over the blade surface is characterized by a strong adverse pressure gradient and flow separation. It usually forms close to the leading edge of the blade and remains attached to the surface as it grows in size. The dynamic behavior of the sheet is driven by variations in the upstream inflow, and its induced pressure disturbances are typically aligned with the Blade Passing Frequency (BPF) and its harmonics. Tip vortex cavitation develops near the blade tip but is not necessarily attached to the

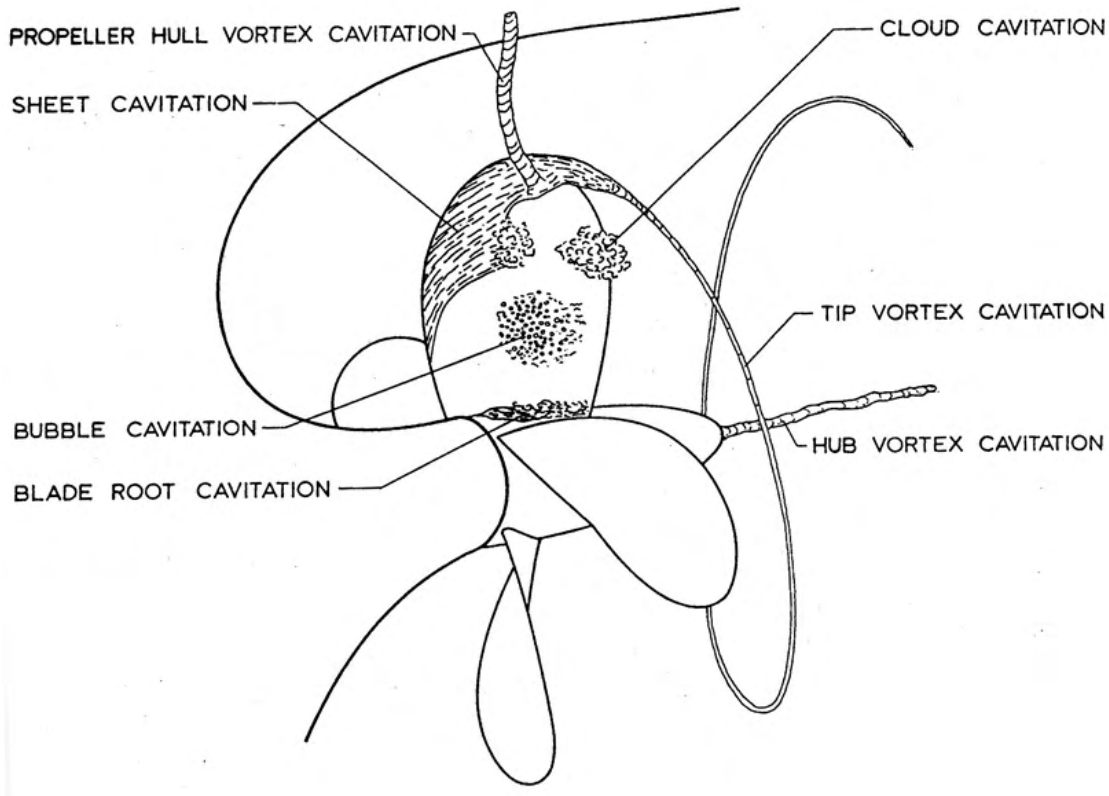

Figure 1.4: Common types of cavitation on marine propellers [10].

surface. Instead, it develops within the core of a vortex structure, which are typically more unstable and dynamic, making them a significant source of high-frequency noise.

Propeller noise, especially under cavitating conditions, is generally considered the dominant contributor compared with hydrodynamic and machinery sources. The characteristics of an idealized radiated noise signature from a propeller for non-cavitating (wetted) and cavitating conditions are shown in Figures 1.5 and 1.6, respectively. For wetted flow, the lower frequencies are characterized by tonal components, which are peaks aligned with the BPF and its harmonics. These are primarily caused by disturbances from the blade thickness and rotation. At higher frequencies, the noise becomes broadband and is associated with pressure fluctuations over the blade surface and turbulence. Under cavitating conditions, the noise signature remains similar at lower frequencies, but higher levels occur due to the collapse of vapor structures such as sheet cavitation. On the other hand, higher frequencies become characterized with a hump that is associated with the dynamics and collapse of the tip vortex structures.

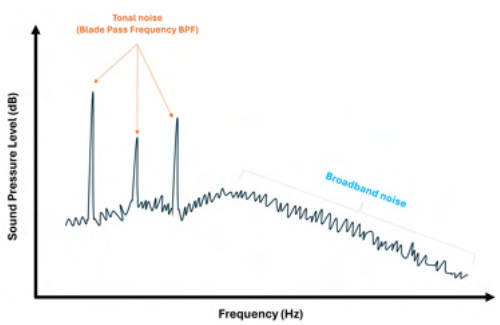

Figure 1.5: Idealized noise spectra from a non-cavitating propeller.

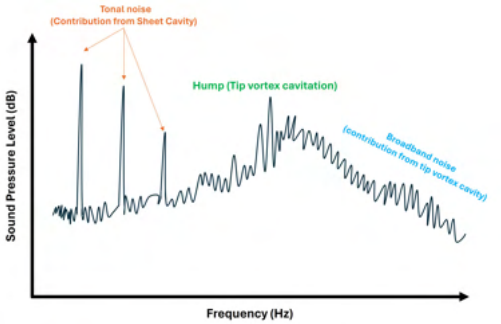

Figure 1.6: Idealized noise spectra from a cavitating propeller.

1.3 Challenges with Cavitation and Noise Assessment

As cavitation is associated with many adverse effects, it is an important parameter to consider during the design and operational phases. Currently, numerical simulations and model scale tests are most widely used for these purposes.

There is a long history of continuous development for best practices and guidelines by the International Towing Tank Conference (ITTC) for model scale tests. To obtain representative results relative to full scale, an important first step is to ensure performance similarity through torque K_Q or thrust K_T coefficients, which are defined as,

$$K_T = \frac{T}{\rho n^2 D^4}, \tag{1.1a}$$

$$K_Q = \frac{Q}{\rho n^2 D^5}, \tag{1.1b}$$

where T is propeller thrust, ρ is water density, n is propeller rotation rate, D is propeller diameter, and Q is propeller torque. In addition to loading similarity, the procedure includes the cavitation number (σ) to match pressure conditions and achieve inception similarity,

$$\sigma = \frac{P_\infty - P_v + P_h}{0.5\rho(nD)^2}, \tag{1.2}$$

where P_∞ is the reference static pressure, P_v is the vapor pressure of water, and P_h is the hydrostatic pressure at a given vertical position.

Even with careful considerations for these parameters, experiments suffer from several other limitations that affect their reliability. One of the main challenges is the impracticality of achieving similarity for the Reynolds number [11]. This results in disparities in viscous effects and boundary layer development when compared to full scale conditions [11]–[14]. The problem is a well-known limitation within the research community and its consequences are referred to as scale effects. These variations influence the wakefield distribution upstream

of the propeller disc, changing the spatial and temporal loading on the blades [15]. In addition, as model scale propellers typically operate at relatively low Reynolds numbers, the laminar boundary layer on the blade surface suppresses or delays cavitation development [16], making it often appear unstable and intermittent [17]. Therefore, if tests are conducted on the same geometry with identical K_T and σ but at different Reynolds numbers, discrepancies in the observed cavitation are expected.

Apart from limitations in achieving Reynolds number similarity, cavitation behavior is also dependent on the geometric scaling. The cavitation number similarity between model and full scale propellers is typically achieved at one specific position. The ITTC recommends this position to be close to the blade tip [18]. However, due to the larger scale and greater depths full scale, the contribution from the hydrostatic pressure component is more significant. This results in disparities in the cavitation numbers along the blade span between model tests and full scale conditions, affecting cavitation inception [13]. In addition, geometrically larger bodies tend to generate broader low-pressure zones, which increases the likelihood of nuclei destabilizing and initiating cavitation, making full scale propellers more prone to cavitation [19]. Furthermore, the differences in time and velocity scales will affect cavitation behavior as higher velocities enhance dynamic pressure fluctuations, which lowers the threshold for nuclei destabilization [19]. Finally, water quality and nuclei concentration are also a significant challenge in model scale testing. The presence of nuclei allows for cavitation to occur at higher pressure levels than would be possible in pure water [20], [21]. As a result, variations in nuclei between testing facilities can lead to differences [22], [23], influencing the reliability and repeatability of the tests.

Numerical studies on scale effects are also challenging and remain scarce within the research community. Most available literature for cavitation at full scale conditions is for stand-alone propellers with uniform or non-uniform inflow conditions. Investigations on scale effects indicate that larger cavitation extent is observed with higher Reynolds numbers [24] [25]. However, these studies do not account for the scale effects on the dynamic behavior of the wakefield and its impact on the cavitation. In addition, one of the most common challenges with these simulations is associated with resolving the tip vortex dynamics [26]–[29]. Overall, there is still a big research gap in understanding scale effects on cavitation for propellers operating in-behind conditions.

Experimental investigations for scale effects on underwater radiated noise are also limited. One of earliest studies is reported in [30] where large discrepancies are found between model and full scale measurement campaigns. Similar observations were made by [31] where the unstable sheet cavitation in model tests influenced the lower frequency levels. In contrast, [32] found good agreement at lower frequencies but reported significant differences for higher frequencies, as also reported in [29]. Although model tests are common in the research community, the noise measurements are influenced by factors other than scale effects, including background noise and reverberations [23]. As acoustic reverberations from the tunnel walls will interfere with the true noise signal, tailored transfer functions for the cavitation tunnels must be determined

to correct for these effects [33]. An example of the challenge in model scale noise measurements is presented in [23], where large discrepancies were found between different facilities, even though observations of cavitation patterns were in reasonable agreement.

For URN numerical predictions, the Ffowcs Williams–Hawkings (FW-H) acoustic analogy [34] is widely used [35]–[37]. While best practices for hydroacoustic applications have been summarized in [38], the combination of the acoustic analogy with a permeable data surface for hydroacoustic applications presents many challenges. A known issue is the end-cap problem, which causes spurious spikes in the predicted noise signal when undamped volume sources exit the integration surface [39]. To mitigate this effect, proposed solutions include a dynamic technique [39] or removal of surface closures in the upstream and downstream regions [35], [38]. In addition, erroneous URN predictions have been reported for a non-cavitating propeller when the permeable FW-H approach is combined with an incompressible flow input [40]. In a later study for a cavitating propeller, it is found that the source of the erroneous predictions are due to induced artificial directivity as computed pressure at a given position and time on the integral surface represents all sources contributions without accounting for phase shifts [41]. The accumulation of source contributions leads to erroneous noise levels, particularly at high frequencies. Similar observations were made by [42], who further investigated the issue and found that the predictions are sensitive to the shape and size of the permeable data surface. These studies show that reliable numerical predictions of underwater radiated noise remain a big challenge within the research community.

1.4 Main Objectives of the Research

The primary objective of this research is to investigate numerical predictions for underwater radiated noise from a full scale cavitating propeller and to assess the associated scale effects. The goals are organized into three main categories:

- **Scale effects on cavitation**: This research aims to investigate scale effect on cavitation using Computational Fluid Dynamics (CFD) simulations. For this purpose, two test cases featuring different types of cavitation have been selected:

  The first test case involves the Delft Twist11 hydrofoil shown in Figure 1.7 (left), which is characterized by unsteady cloud shedding behavior. The analysis focuses on pressure distribution, cloud cavitation shedding dynamics, and modal decomposition of the vapor cloud using Proper Orthogonal Decomposition (POD). Numerical results are compared with model scale experiments conducted in the cavitation tunnels at Delft University of Technology (TU Delft) and the École Polytechnique Fédérale de Lausanne (EPFL).

  The second test case involves a propeller shown in Figure 1.7 (right), that is operating in the wake field of a ship hull. Sheet and tip vortex cavitation are observed for this test case. Scale effects on the wakefield distribution,

cavitation development and dynamics, induced pressure fluctuations, and pressure pulse levels are investigated. Results are compared against model scale tests performed in the cavitation tunnel at the Research Institutes of Sweden (RISE).

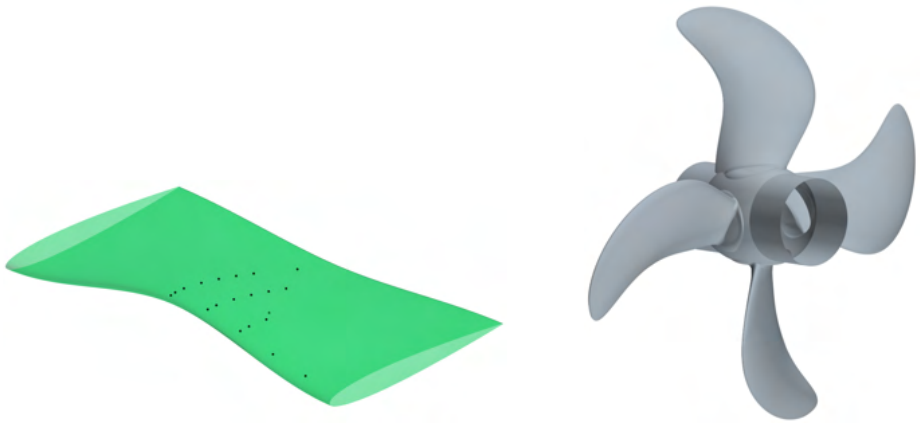

Figure 1.7: Delft Twist 11 hydrofoil geometry (left) and propeller geometry (right).

- **Blockage effects on cavitation:** In addition to scale effects, the influence of blockage (domain size) on the cavitating propeller is investigated using two computational domains shown in Figure 1.8. The first matches the dimensions of the cavitation tunnel used in model scale tests and is labeled Tunnel Section (TS). The second is labeled Large Domain (LD) and extends boundaries in all directions far from the ship model. The analysis focuses on wakefield distribution, transient load distribution on propeller blades, cavitation dynamics, induced pressure fluctuations, and pressure pulse levels.

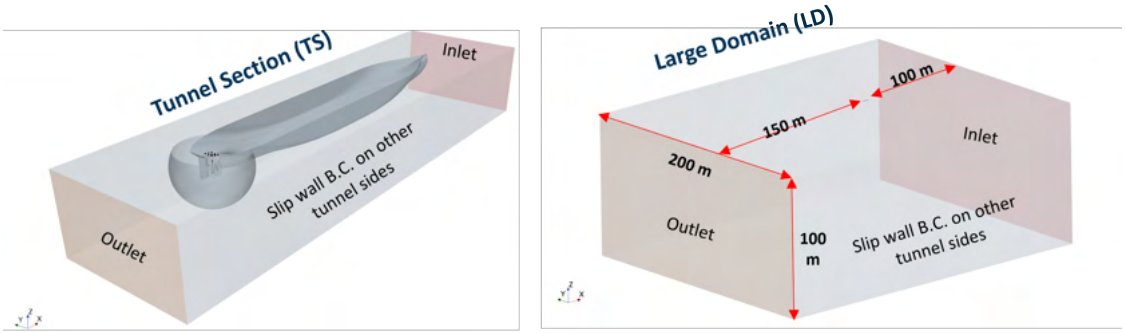

Figure 1.8: Computational domains for the analysis on the blockage effect: Tunnel Section (left) and Large Domain (right).

- **URN Prediction Methodology of a Cavitating Propeller:** Reliable numerical predictions of underwater radiated noise from cavitating propellers remain a significant challenge. In the context of noise, one objective of this thesis is to investigate limitations and problems associated with permeable FW-H acoustic analogy in combination with incompressible

flow input. Furthermore, an alternative approach is proposed for predicting cavitation noise, based on monopole source propagation. Further details on this approach are provided in Section 2.3.

1.5 Thesis Outline

Part I of this thesis provides a summary of the research work and results which is divided into four chapters:

- **Chapter 1** presents the introduction, background information, literature review, and objectives of the research work..
- **Chapter 2** outlines the governing equations and numerical methodologies used for the simulations, along with details of the proposed alternative noise prediction approach.
- **Chapter 3** summarizes the results for the investigated cases, focusing on scale and blockage effects on cavitation, as well as URN predictions for a cavitating propeller at both model and full scale conditions.
- **Chapter 4** concludes the thesis with a summary and suggestions for future work.

Part II includes appended papers which provide more details of the research work and findings.

Chapter 2

Numerical Methods

2.1 Continuity and Momentum Equations

The single fluid approach is chosen in this work, where the liquid and vapor phases are treated as a homogeneous mixture. The fluid mixture density ρ_m and dynamic viscosity μ_m are defined as,

$$\rho_m = \alpha_v \rho_v + (1 - \alpha_v)\rho_l \tag{2.1}$$

$$\mu_m = \alpha_v \mu_v + (1 - \alpha_v)\mu_l \tag{2.2}$$

Subscripts m, v, and l correspond to the mixture, vapor, and liquid phases, respectively. An additional transport equation is needed to solve for the volume fraction α as detailed in Section 2.1.2.

Any fluid must satisfy the conservation laws of mass and momentum, and these laws are the basic principles upon which Computational Fluid Dynamics (CFD) is built. In the Reynolds-Averaged Navier–Stokes (RANS) framework, the general formulation of mass conservation for a fluid mixture is expressed as,

$$\frac{\partial(\rho_m)}{\partial t} + \nabla \cdot (\rho_m U_m) = 0, \tag{2.3}$$

where ρ_m is the mixture density and U_m is the average mixture velocity. The fluid must also satisfy the conservation of momentum, which are the Navier–Stokes equations,

$$\frac{\partial(\rho_m U_m)}{\partial t} + \nabla(\rho_m U_m U_m) = -\nabla p + \nabla(\tau - \rho_m \overline{u'u'}) + f \tag{2.4}$$

Here p is the pressure, τ is the viscous stress tensor, f are body forces, and $-\rho_m \overline{u'u'}$ is the Reynolds stress tensor. The Boussinesq approximation is commonly used to model the Reynolds stresses which assumes a linear constitutive relation with the mean strain rate S,

$$-\rho_m \overline{u'u'} = 2\mu_T S - \frac{2}{3}\rho_m k I, \tag{2.5}$$

where μ_T is the eddy viscosity, k is the turbulent kinetic energy, and I is the identity matrix. In all simulations, eddy viscosity is modeled with the $k-\omega$ SST turbulence model [43] which uses the strain rate to calculate the eddy viscosity,

$$\mu_T = \frac{\rho k}{\min(\frac{a^*}{\omega}, \frac{a_1}{SF_2})} \tag{2.6}$$

In this equation, a_1 and a^* are model coefficients, k is the turbulent kinetic energy, ω is the specific dissipation rate, and F_2 is a blending function. Both k and ω are modeled using additional transport equations.

2.1.1 Dynamics of Spherical Vapor Bubbles and Cavitation Modeling

Before presenting the cavitation modeling approach adopted in this work, it is first useful to consider the physics of vapor bubbles and their dynamics. Suppose a vapor bubble exists in a stationary water medium, which is assumed to be spherical with its radius varying in time R(t), as shown in Figure 2.1.

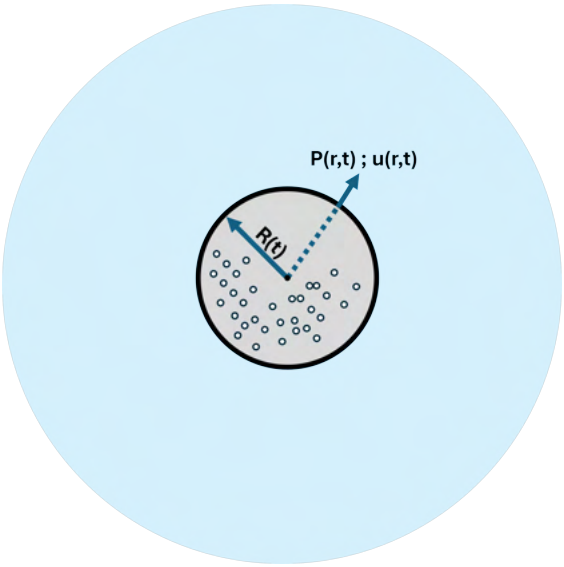

Figure 2.1: Schematic of a spherical vapor bubble in a stationary water medium.

The spatial and temporal evolution of the bubble can be determined by applying the laws of mass and momentum conservation to the interface between the vapor and liquid mediums. The boundary conditions at the interface are represented by a force balance of the normal stresses from the liquid, gas, and vapor phases, which is expressed as,

$$P(R,t) = P_v + P_g(t) - \frac{2s}{R} + 2\mu\frac{\partial u}{\partial r} \tag{2.7}$$

where $P(R,t)$ is the liquid pressure P_v is the vapor pressure within the bubble, $P_g(t)$ is the gas pressure, s is the surface tension, and μ is the dynamic viscosity accounting for viscous effects. Following the law for the conservation of momentum and considering the boundary conditions outlined above, the expression for the evolution of a spherical vapor bubble yields the Rayleigh-Plesset equation,

$$\rho\left[R\frac{d^2R}{dt^2}+\frac{3}{2}\left(\frac{dR}{dt}\right)^2\right]=P_v-P_\infty+p_g-\frac{2s}{R}-4\mu\frac{\dot{R}}{R} \tag{2.8}$$

The terms ρ and P_∞ are liquid density and and far field pressure. The equation describes the spatial and temporal evolution of a spherical vapor bubble and its induced pressure field. For cavitating propellers, inertial forces are typically dominant while viscous and surface tension effects are less significant. This allows to simplify cavitation modeling as detailed in the subsequent Section 2.1.2.

2.1.2 Mass Transfer Modeling

In this work, the single fluid approach is chosen for cavitation modeling. One additional transport equation for the local volume fraction α is needed to solve for the vapor/liquid phases,

$$\frac{\partial\alpha}{\partial t}+\nabla(\alpha u)=\frac{\dot{m}}{\rho}, \tag{2.9}$$

where $\dot{m}$ represents the mass transfer rate source term for vaporization and condensation. The mass transfer rate is modeled using Schnerr-Sauer [44] cavitation model and the volume fraction of vapor α_v is defined as the ratio between the local vapor and the local cell volumes,

$$\alpha_v=\frac{V_v}{V_{cell}}=\frac{n_0\frac{4}{3}\pi R^3}{1+n_0\frac{4}{3}\pi R^3}, \tag{2.10}$$

Here, n_0 represents the initial number of bubbles per unit volume of liquid, and R is the bubble radius. The rate of change of the volume fraction is expressed as,

$$\frac{d\alpha_v}{dt}=\alpha_v(1-\alpha_v)\frac{3}{R}\frac{dR}{dt}, \tag{2.11}$$

the bubble mass transfer rate $\frac{dR}{dt}$ is simplified and the terms accounting for the effects of bubble acceleration, viscous forces, surface tension in the Rayleigh-Plesset Equation 2.8 are neglected. The resulting rate of change for bubble growth and collapse is reduced to,

$$\frac{dR}{dt}=\sqrt{\frac{2}{3}\frac{|P(R)-P_\infty|}{\rho_l}}, \tag{2.12}$$

where $P(R)$ represents the internal pressure of the bubble and P_∞ is the far-field pressure. The mass transfer source term for vaporization and condensation is defined as,

$$\dot{m} = \begin{cases} C_c \frac{\rho_l \rho_v}{\rho_m} \frac{d\alpha_v}{dt}, & \text{if } P(R) > P_v \\ C_v \frac{\rho_l \rho_v}{\rho_m} \frac{d\alpha_v}{dt}, & \text{if } P(R) \leq P_v \end{cases} \tag{2.13}$$

As standard RANS models were originally developed and tuned for applications with single-phase flows, one of their limitations when applying them to multiphase cases is their tendency to predict excessive eddy viscosity levels in mixture regions [45]. This is particularly relevant in cases of shedding cloud cavitation where the excessive eddy viscosity suppresses the formation of the re-entrant jet, which is a mechanism important for unsteady cavity dynamics [46], [47]. To address this limitation, the Reboud correction [45] is applied in this work, which modifies the eddy viscosity in the mixture region,

$$f(\rho) = \rho_v + \left(\frac{\rho_v - \rho}{\rho_v - \rho_l} \right)^n (\rho_l - \rho_v), \tag{2.14}$$

where n is a constant set to the recommended value of 10, and the correction is only active in the mixture regions.

2.2 Ffowcs Williams-Hawkings Acoustic Analogy

During the 1950s, Lighthill was interested in computing the noise emissions from jet engines. He realized that the assumption made to derive the linear acoustic wave equation, which states that perturbations of pressure and density are much smaller than the mean quantities, is not valid in cases of highly turbulent flows where non-linear interactions are present. He reformulated the continuity and momentum equations to derive an inhomogeneous wave equation, which is known as the Lighthill Acoustic Analogy [48], [49]:

$$\frac{\partial^2 \rho'}{\partial t^2} - c_\infty \frac{\partial^2 \rho'}{\partial x_i^2} = \frac{\partial^2 T_{ij}}{\partial x_i \partial x_j}; \tag{2.15}$$

here, ρ' is the density perturbation, c_∞ is the speed of sound. The additional term T_{ij} is the Lighthill stress tensor which accounts for the non-linear interactions for sound generated from turbulent flow in a stationary medium,

$$T_{ij} = \rho v_i v_j + P_{ij} - c_\infty (\rho - \rho_\infty) \delta_{ij} \tag{2.16}$$

where P_{ij} is the compressive stress tensor to account for pressure and viscous forces. Later in 1955, Curle extended the Lighthill's solution to account for the presence of stationary solid surfaces by adding additional terms based on wall normal velocity to the surfaces [50].

In 1969, Ffowcs Williams and Hawkings extended the work of Curle to account for the sound generated from surfaces in arbitrary motion [34]. The

solution uses the concept of generalized derivatives and a Heaviside function H_s to define the moving surfaces. By using the method of Green's function, the solution to the inhomogeneous wave equation in an infinite domain becomes,

$$P'(x,t)H_s = P'_T(x,t) + P'_L(x,t) + P'_Q(x,t) \tag{2.17}$$

where $P'_T(x,t)$ is the thickness term which describes contributions from the monopole sources,

$$P'_T(x,t) = \frac{1}{4\pi}\frac{\partial}{\partial t}\int_S \left[\frac{(\rho v_j - \rho' V_j)n_j}{r|1-M_r|}\right]_{ret} \tag{2.18}$$

In more detail, the term states that a monopole wave is generated when there is a mass flux across a surface $\rho v_j n_j$ or due to the displacement of medium because of the surface motion $\rho' V_j n_j$ such as a rotating propeller. This term would be zero for a stationary surfaces. Also, It is worth noting that the term $\rho v_j n_j$ would be zero for an impermeable solid surface.

The second term $P'_L(x,t)$ is the Loading term which describes the contributions from the dipole sources,

$$P'_L(x,t) = -\frac{1}{4\pi}\frac{\partial}{\partial x_i}\int_S \left[\frac{(\rho v_i(v_j - V_j) + P_{ij})n_j}{r|1-M_r|}\right]_{ret}, \tag{2.19}$$

this term is dominated by the pressure forces within the compressive stress tensor P_{ij}, and the contributions from the viscous component are small. Again, the term $\rho v_i v_j$ would be zero for impermeable surfaces.

$P'_Q(x,t)$ is the quadrupole term which describes the sound generated by non-linear interactions and turbulence,

$$P'_Q(x,t) = \frac{1}{4\pi}\frac{\partial^2}{\partial x_i x_j}\int_V \left[\frac{T_{ij}}{r|1-M_r|}\right]_{ret} \tag{2.20}$$

here, T_{ij} is the Lighthill stress tensor as described in Equation 2.16. In the context of this work, the volume integral of quadrupole term is dropped with the assumption that the noise contributions are small compared to the other components. In addition, an advantage of neglecting this term is reducing the computational cost.

It is worth stating that the expression in Equation 2.17 is derived based on the following assumptions:

- The acoustic analogy is developed for single-phase and compressible medium which allows for the propagation of acoustic waves.
- The solution is obtained using free-field Green's function. This implies that the domain is infinite and bounds the noise sources without reflections.
- The obtained wave equation is inhomogeneous and linear, meaning that it is applicable for far-field acoustic predictions.

2.3 Cavitation as a Monopole Noise Source

Given the limitations associated with the application of the FW-H acoustic analogy for hydroacoustic applications discussed in Section 1.3, part of the purpose of this research is to propose an alternative prediction methodology. Since cavitation noise is typically considered the dominant source in the context of URN from ships, the idea is to treat cavitation as a monopole source, and the solution starts with the wave equation,

$$\nabla^2 P = \frac{1}{c^2}\frac{\partial^2 P}{\partial t^2} \tag{2.21}$$

where ∇^2 is the Laplace operator, P is the acoustic pressure, and c is the sound speed. If we consider a sound wave in a spherical coordinate system under the assumption that the wave fronts are spherical (i.e. flow variables such as pressure and velocity are dependent only on the radial distance), the solution to the simplified wave equation becomes,

$$P(r,t) = \frac{1}{r}f(ct-r) + \frac{1}{r}g(ct+r) \tag{2.22}$$

here, f and g represent forward and backward moving acoustic waves. It is important to note that the wave amplitude decays by a factor of $\frac{1}{r}$ as it propagates in distance. Simplifying the expression further by neglecting backward moving waves (such as reflected ones), and assuming Harmonic Time Dependence where waves are linear and in combination with Euler's equation, the solution to a pulsating monopole source is [51],

$$P(r,t) = \frac{\rho}{4\pi r}\ddot{V}\left(t - \frac{r}{c}\right) \tag{2.23}$$

where r is the distance between the source and receiver, and $\ddot{V}$ is the second order derivative of the source volume. It is important to highlight that the solution for Equation 2.23 is obtained under the following assumptions:

- The wavefronts are assumed to be spherical with flow variables such as pressure and velocity being uniform over a given spherical surface.
- Only a forward propagating wave is considered, meaning the solution is for an infinite medium and reflected waves are neglected.
- The derivation assumes linear acoustics (small-amplitude waves) and neglects nonlinear effects.
- The source is compact as the diameter of the spherical source is assumed to be much smaller than the wavelength.
- It is valid for far-field predictions where the diameter of the spherical source is much smaller than the distance to the receiver.

2.4 Compressible vs Incompressible Flow Input

The propagation of acoustic waves is enabled by the compressible nature of the medium, as density perturbations allow for the acoustic wave to travel in space and time. Therefore, to accurately resolve the wave propagation in numerical simulations, one must account for the medium compressibility.

In hydroacoustic applications where large scales are considered, it is computationally unfeasible to satisfy the numerical constraints for a proper fully compressible solution. Therefore, given the computational limitations, the incompressible assumption is used in all of the simulations in this work. This means that acoustic wave propagation is not resolved by the CFD simulation, and pressure disturbances propagate at an infinite speed when collected by the FW-H surface. As a result, the phase shift between the different source is not captured. However, the incompressibility assumption can be valid for low Mach number flows in which compressibility effects are negligible [52], [53]. Although the assumption of incompressibility is adopted in this work, potential limitations and problems are acknowledged as discussed in Section 1.3.

Chapter 3

Summary of Results

3.1 Scale Effects on a Cavitating Hydrofoil

General Description

The Delft Twist 11 hydrofoil is chosen for this test case which has a geometrical profile based on the NACA0009 with a chord length of 150 mm and a span of 300 mm at model scale. The geometry is unique in its design with a symmetric spanwise variation in the angle of attack (AOA) from 0^o at the sides to 11^o at the centerline. The gradual increase in the angle of attack induces load variations, resulting in the development of a three-dimensional cavity. The cavitation on the Delft Twist 11 hydrofoil is characterized by unsteady cloud shedding behavior, and the analysis primarily focuses on the influence of scale on cavitation. The Large Scale (full scale) simulations are performed using a geometrically scaled-up model with a ratio of $\lambda = 20$. Results are compared with model scale tests done at Delft University of Technology (TU Delft) [54] and École Polytechnique Fédérale de Lausanne cavitation tunnels.

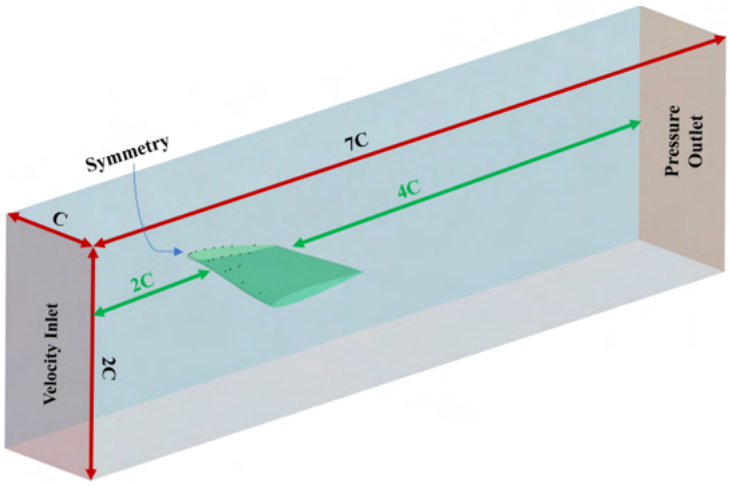

Figure 3.1: Computational domain and boundary conditions for the Delft Twist 11 hydrofoil.

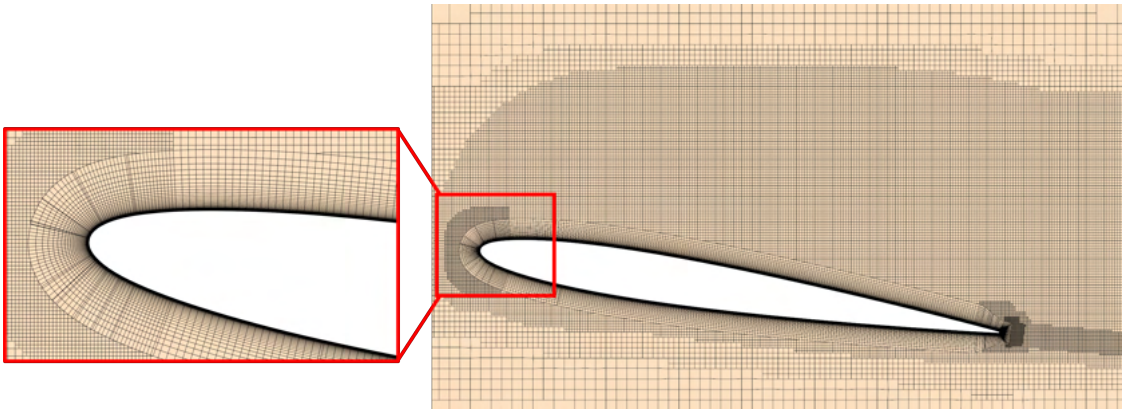

Figure 3.2: Cross-section view of the generated grid for Delft Twist 11 hydrofoil

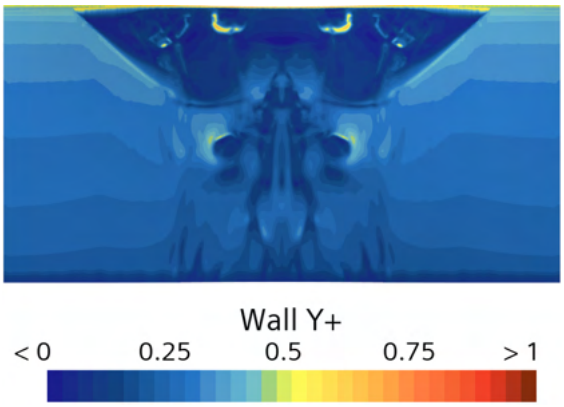

Figure 3.3: Distribution of y^+ values at a random instance on the hydrofoil upper side at model scale.

The computational domain designed for this test case is shown in Figure 3.1. The hydrofoil is placed two chord lengths from the inlet and four chord lengths from the outlet. Slip wall boundary conditions are applied to the top, side, and bottom walls, with a symmetry boundary condition imposed at the centerline plane. All simulations are performed using the commercial software package Simcenter STAR-CCM+, and domain is discretized using the built-in trimmer mesher as shown in Figure 3.2. The grid resolution is refined on the upper side and is extended in the downstream direction to capture the dynamics of the transported cloud cavity. To properly resolve the gradients within the boundary layer, a mean y^+ value below 1.0 is maintained for both model and full scale simulations and an example for the y^+ distribution is shown in Figure 3.3 for model scale condition.

Results

Numerical predictions of the pressure distribution on the upper side, averaged over 15 shedding cycles, are presented in Figure 3.4 at 40% and 50% of the span along with experimental measurements. While numerical predictions show acceptable agreement with the EPFL measurements, greater differences are obtained when compared to the TU Delft measurements. The greater

discrepancy is possibly associated with uncertainties from the experiments as the tests were performed at similar conditions. Regardless, the numerical simulations overpredict pressure levels at both span locations, which influences the extent of the developed attached cavity. On the scale effects, the pressure levels are lower at the full scale condition near the cavity closure region ($0.45 < x/C < 0.55$). It is also interesting to note the gradual increase in pressure level by the numerical predictions from the leading edge up to 0.15 x/C at both model and full scale conditions at 0.5 Span, which likely associated with the momentum loss of the re-entrant jet as it travels to the leading edge.

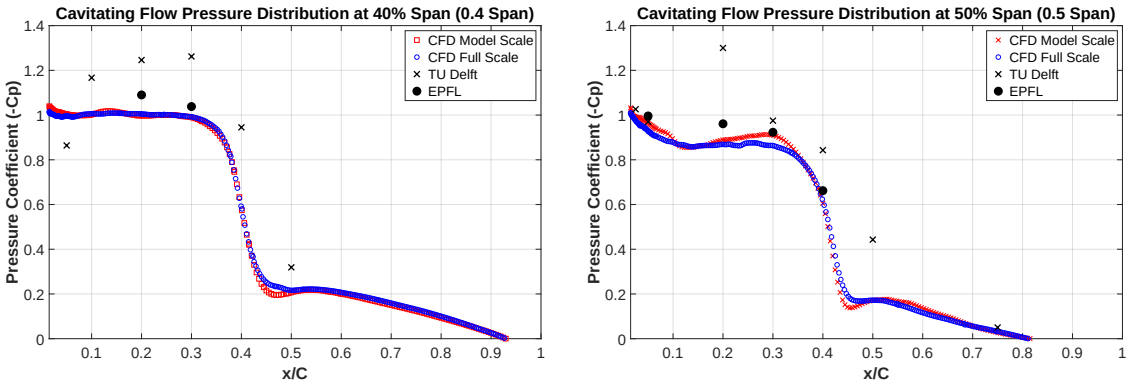

Figure 3.4: Pressure distribution on the Delft Twist 11 upper side: 40% span (left) and 50% span (right).

Predicted cavitation dynamics and shedding is provided at different time instants for one typical shedding cycle in Figure 3.5. Snapshots for model and full scale simulations are presented together with experiments from TU Delft. The cavitation structures are visualized using an iso-surface set at $\alpha_v = 0.5$. Vortical structures show the normalized Q-criterion, and the limiting streamlines represent the vector direction of the wall shear stress. The overall behavior of the cavitation dynamics and shedding mechanisms are in good agreement between the numerical results and experiments. A side-entrant jet appears in the first four snapshots, which is characterized with small-scale vortices that remove and entrain vapor structures in the downstream direction. Numerical predictions underpredict the volume of the entrained vapor, which could be attributed to many factors including overprediction of pressure levels, the RANS approach, and spatial resolution. The scale effect on the attached cavity shows that the sheet extends slightly longer at the full scale condition, which is inline with the predicted averaged pressure levels.

The fourth snapshot shows the time instant at which the sheet detached from the foil surface due to the re-entrant jet traveling upstream to the leading edge. At this instant, the detachment at the full scale condition has already started, while this is delayed at model scale as the re-entrant jet has not yet reached the leading edge. As the sheet detaches from the foil surface, the vapor structures form a cloud that travels in the downstream direction as shown in the sixth time instant. The cloud is characterized by a spanwise vortex structure at both model and full scale conditions. A wall normal secondary vortex starts to develop in the seventh snapshot, which later evolves into a

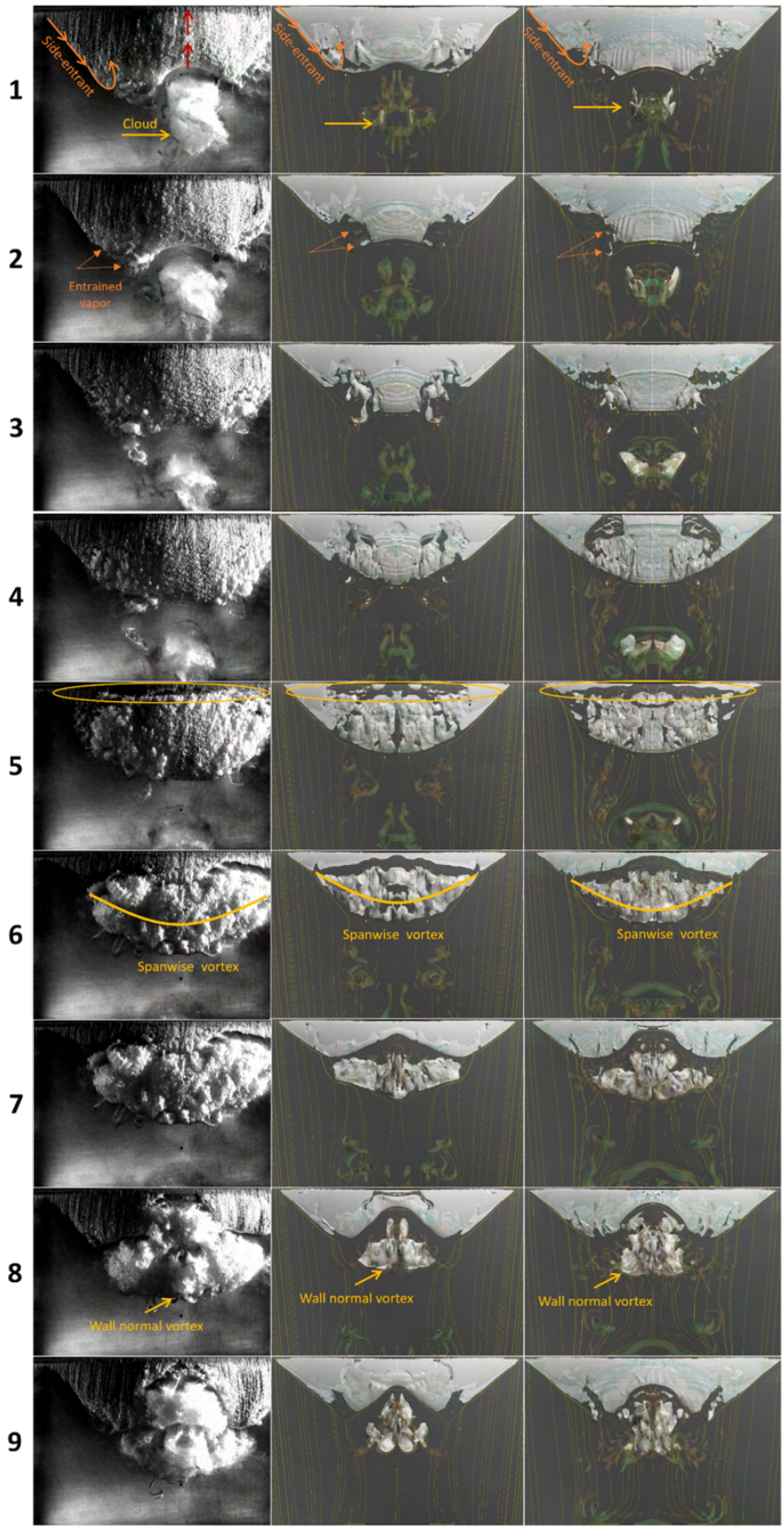

Figure 3.5: Instantaneous snapshots for the time evolution of the shedding cloud.

horse-shoe structure that carries vapor within its core as shown in the last two snapshots. While the irregular nature of the cloud makes averaged observations of scale effects difficult to obtain, it appears that scale effects do not change the global behavior or shedding mechanism of the cloud. However, they are more pronounced on smaller scale vortical structures, which is due to the higher Reynolds number and broader energy spectrum.

The Fast Fourier Transform FFT is applied to the collected vapor volume to identify the shedding frequency of the cloud. Good agreement is obtained between the model scale simulations and experiments as the computed shedding frequency is 32.48 Hz and 32.5 Hz, respectively. This corresponds to a Strouhal number of 0.699 at model scale. At full scale, the predicted shedding frequency is 1.89 Hz, resulting in a Strouhal number of 0.71, which indicates to a shift due to the scale effects on the re-entrant jet.

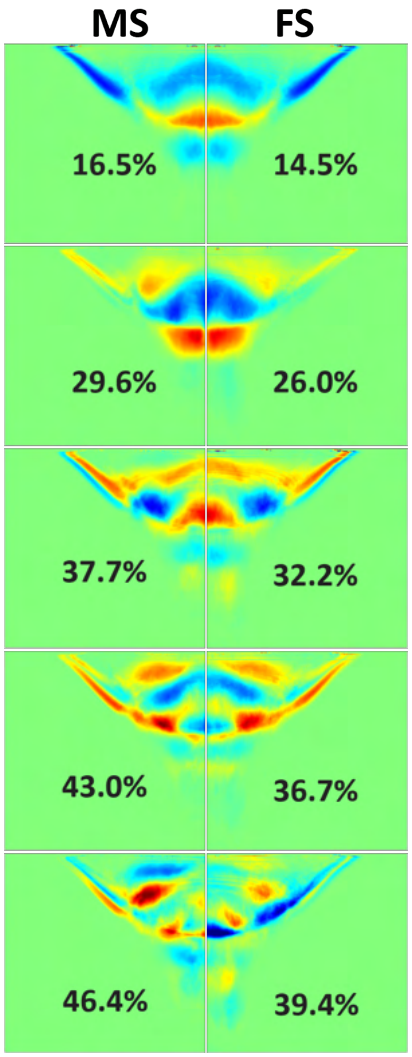

Figure 3.6: Dominant POD spatial modes 1 through 5 (Percentages represent cumulative energy).

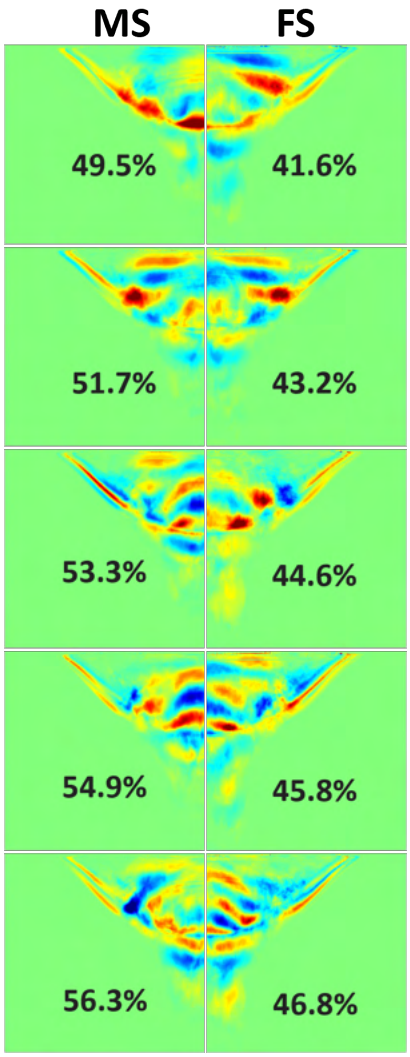

Figure 3.7: Higher-order POD modes 6 through 10 (Percentages represent cumulative energy).

To further investigate scale effects on cavitation, modal analysis is performed on two-dimensional snapshots of the transient cavitation using Proper Orthogonal Decomposition (POD). The decomposition allows to visualize coherent and dominant spatial structures which contribute to the highest energy, and identify the corresponding key dynamics of the cloud shedding . Figure 3.6 presents the obtained first five spatial modes for both model and full scale conditions. The percentages represent the cumulative energy contribution relative to the total energy. The first two modes reveal that the large-scale spanwise vortex and horse-shoe structures are dominant and contribute the highest energy. In addition, the side entrant jet and its interactions with the attached cavity is also highly dynamic. Smaller-scale vapor structures are observed after the second mode including vortices associated with the transported cloud. Since first four modes are almost identical at both scales, the results suggest that large-scale structures are not significantly influenced by scale effects. Finally, it is worth noting that lower percentages of the cumulative energy distribution is obtained at full scale due to the broader energy distribution across the spectrum of the spatial modes.

While large-scale structures are not influenced by scale effects, higher-order spatial modes presented in Figure 3.7 indicate otherwise. For instance, differences appear near the leading edge and further downstream in the vicinity of the trailing edge in the last three presented modes, where more isolated structures are present. While this is associated with the Reynolds number, it also indicates that on average, the cloud is transported further downstream at full scale due to enhanced mixing effects from the small-scale structures. In summary, scale effects are more pronounced in small-scale structures while the shedding mechanism and dominant structure remain similar.

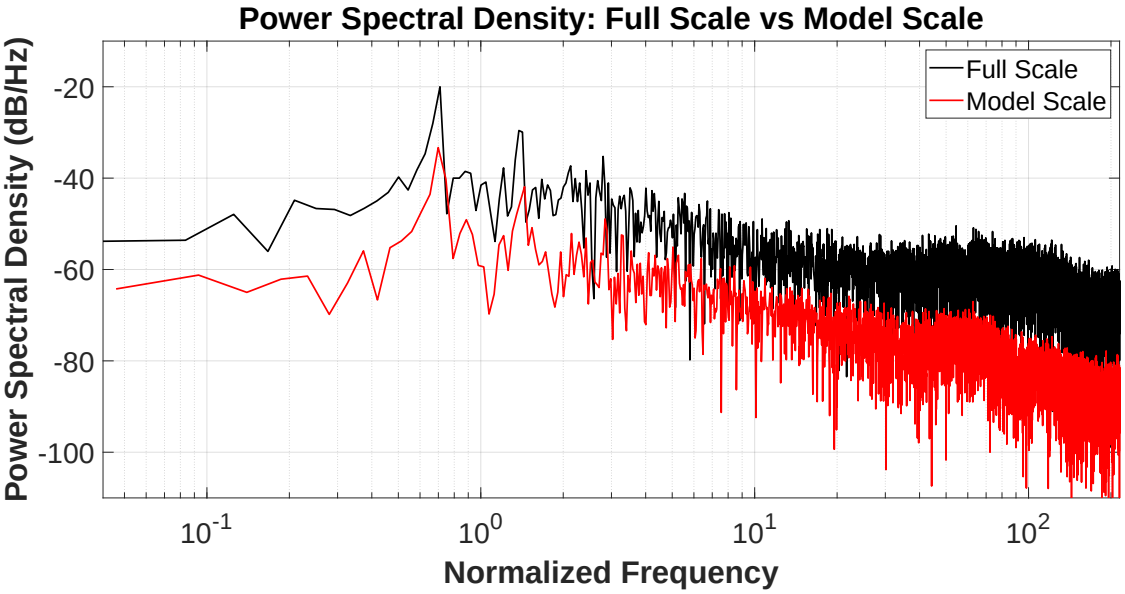

Figure 3.8: Power spectral density of the induced hydrodynamic pressure fluctuations at model and full scale conditions.

Pressure fluctuations history is collected using three virtual transducers that are mounted on the top wall of the computational domain at the midspan of the

foil and located at 10%, 50%, and 100% of the chord length. Data is collected over 15 shedding cycles and normalized to obtain the pressure coefficient. FFT is applied to the pressure coefficient data to compute the Power Spectral Density (PSD) in decibels per Hertz (dB/Hz), and frequency is normalized for consistent comparison between model and full scale conditions as shown in Figure 3.8. Data from the virtual transducer positioned at the mid chord is only presented here. Results indicate the influence of scale effects on the energy content of the pressure fluctuations which is greater at the full scale condition across the entire frequency spectrum. The first peak in the signal corresponds to the predicted shedding frequency with difference of approximately 15 dB/Hz, which is slightly shifted between both scale conditions. In addition, the overall power is higher at full scale, suggesting a more energetic and intense cavitation collapsing events.

3.2 Scale and Blockage Effects on a Cavitating Propeller Operating In-Behind

General Description

This test case is for a moderately skewed, controllable-pitch, four-bladed propeller which is mounted behind the hull as shown in Figure 3.9 (Left) from the model tests performed at the RISE cavitation tunnel. Due to operational constraints in experiments, it was not possible to replicate the the full scale Continuous Service Rating (CSR) condition. As a result, two sets of model scale numerical simulation are performed which match both the experimental and CSR conditions.

Figure 3.9: Ship mounting in RISE cavitation tunnel (left) and top view for the pressure transducers placement during the model tests.

The computational domain for the model scale simulation is sized to match the RISE cavitation tunnel, while the full scale domain is extended to mitigate the influence of boundaries on the solution. Blockage effects caused by the confined space of the tunnel section are investigated for the CSR condition using a larger domain that extends the domain walls away from the model ship. The smaller and large domains are named Tunnel Section (TS) and Large Domain (LD), respectively.

The built-in meshing tools in Star-CCM+ are used to discretized the computational domains. The trimmer mesher is applied to generate predominantly hexahedral cells in all regions except for the rotating one. The Polyhedral and Advancing Layer Mesher (ALM) is applied to the rotating region and propeller, which generates polyhedral cells within the core region but allows for for better control over prism layer quality around the blade surfaces. A mean y^+ value below 1.0 is maintained to resolve the gradients within boundary layer on the propeller and hub. However, the wall function approach is adopted for the hull and rudder at full scale condition. Figures 3.10 and 3.11 show plane-cut view of the generated grid within the rotating region and obtained y^+ distribution on the propeller blades at the full scale condition, respectively.

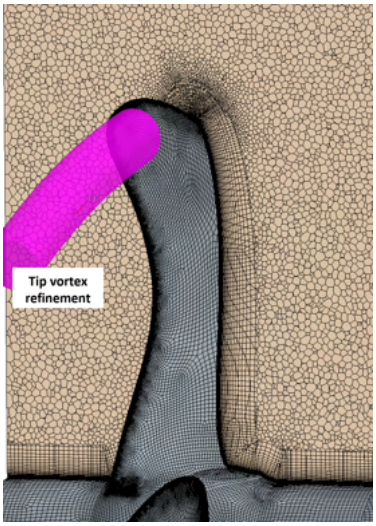

Figure 3.10: Cross-section view of the generated grid for the propeller and rotating region.

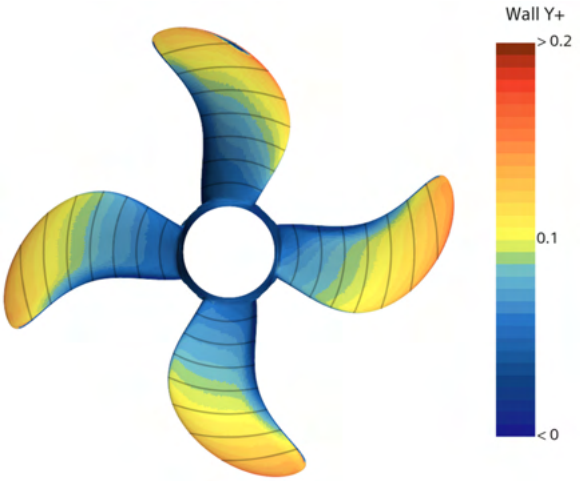

Figure 3.11: Distribution of y^+ values on the propeller blade surfaces.

Figure 3.12 shows the predicted axial velocity distribution, normalized by the free stream velocity, at a cross-sectional plane located at 0.48R upstream of the propeller plane for both model scale (Tunnel Section and Large Domain) and full scale conditions. Strong influence of blockage and scale effects is observed in all radial positions. Regarding scale effects, the influence is due to the difference in the development and thickness of the boundary layer. As a result, the velocity deficit at the wake peak region is much smaller at the full scale condition as shown on the right hand side of the figure. At the model scale Tunnel Section (TS), the wakefield is affected by the blockage as velocity field distribution is modified for all positions when compared with the Large Domain (LD). The flow is accelerated around the hull and into the propeller plane due to the space constraints from the tunnel side and bottom walls. This is more significantly pronounced in the region at the angular positions between 90^o and 270^o, as the wakefield is broader with the LD condition. While the LD condition provides a closer approximation of the full scale wakefield, scale effects remain significant enough to influence the velocity distribution.

To investigate the influence of blockage on propeller loading, Figure 3.13 presents the pressure distribution on the blade's suction side (top) and back side (bottom) for both TS and LD conditions, along with limiting streamlines of wall shear stress vectors. While flow behavior over the blade suction side remains similar between the TS and LD conditions, more significant differences occur on the pressure distribution. Lower pressure levels are obtained for the TS condition, which will influence cavitation inception in regions where pressure level drops below the vapor pressure pressure threshold. The pressure distribution on the back side is also influenced by blockage for all angular positions, which is higher for the LD. In addition, a vortex structure develops on the back side beyond 90^o and starting at radial position 0.5R. The vortex

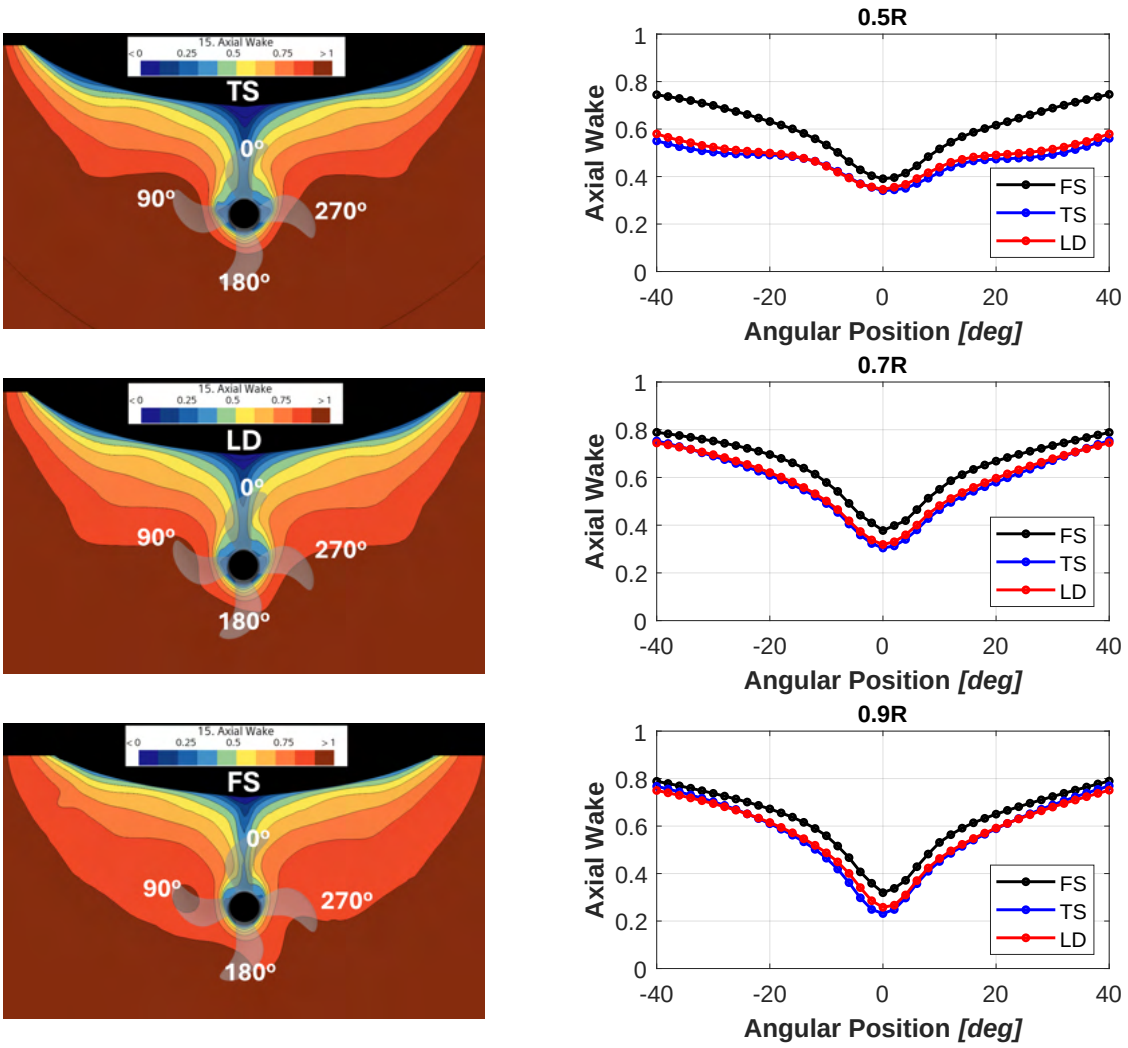

Figure 3.12: Axial wakefield distribution on a cross-section positioned 0.48R upstream the propeller plane for Tunnel Section (TS), Large Domain (LD), and Full Scale (FS) conditions. Right-hand side show the wake distribution at radial positions 0.5R, 0.7R, and 0.9R, where R is the propeller radius.

becomes more pronounced at the 180^o and 270^o positions and is stronger in the TS as indicated by larger pressure drop in that region, leading to more significant performance losses.

Sketches of the observed cavitation patterns during the experimental tests are compared with numerical predictions in Figure 3.14, including the CSR condition. In the numerical results, cavitation is represented with an isosurface defined by $\alpha_v = 0.5$. The figures show blade positions starting at 0^o (the 12 o'clock position), and rotating clockwise as viewed from upstream. Sheet cavitation develops on the blade surface as it enters the wake peak region at 0^o. The surface appears smooth in both experiments and numerical predictions, though discrepancies in the inception point near the leading edge are present. For the CSR condition, scale and blockage effects are pronounced as cavitation extent is largest for the TS condition, followed by the large domain and full scale conditions. As the blade reaches 10^o, the sheet cavitation continues to

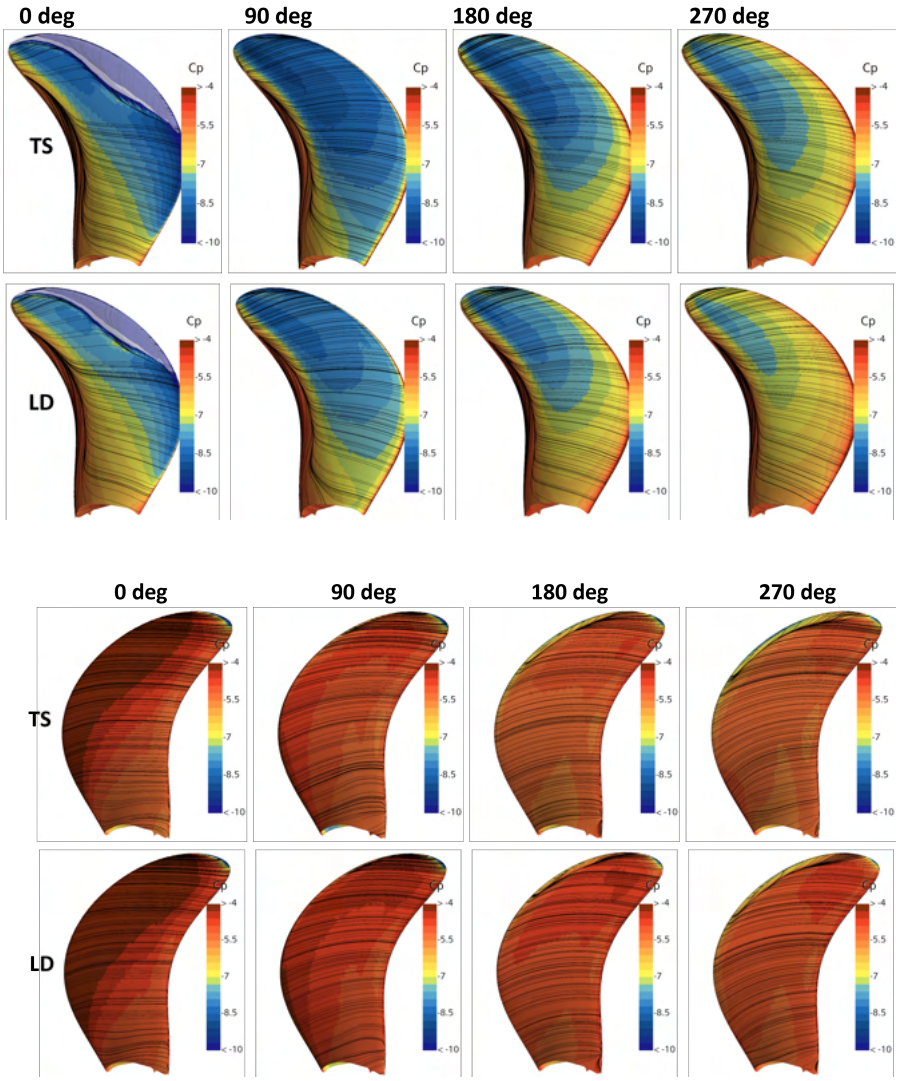

Figure 3.13: Pressure distribution on the blade suction (top) and back (bottom) sides at model scale for Tunnel Section and Large Domain conditions. Limiting streamlines shown on black represent the vector direction of the wall shear stress and cavitation is visualized with iso-surface $\alpha_v = 0.5$.

grow and is charachterized by and uneven surface with convex shape at the closure region, which similarly observed between the experiments and numerical predictions. After exiting the wake peak at 20^o, the sheet begins to collapse and a tip vortex structure develops, which becomes more prominent by 30^o. The tip vortex is highly dynamic with multiple growth and collapse events beyond the 40^o position. In summary, both scale and blockage effects influence the development and dynamics of cavitation, with scale effects being more significant. This is associated with the differences in the wake distribution and the transient loading on the propeller blades between the different conditions.

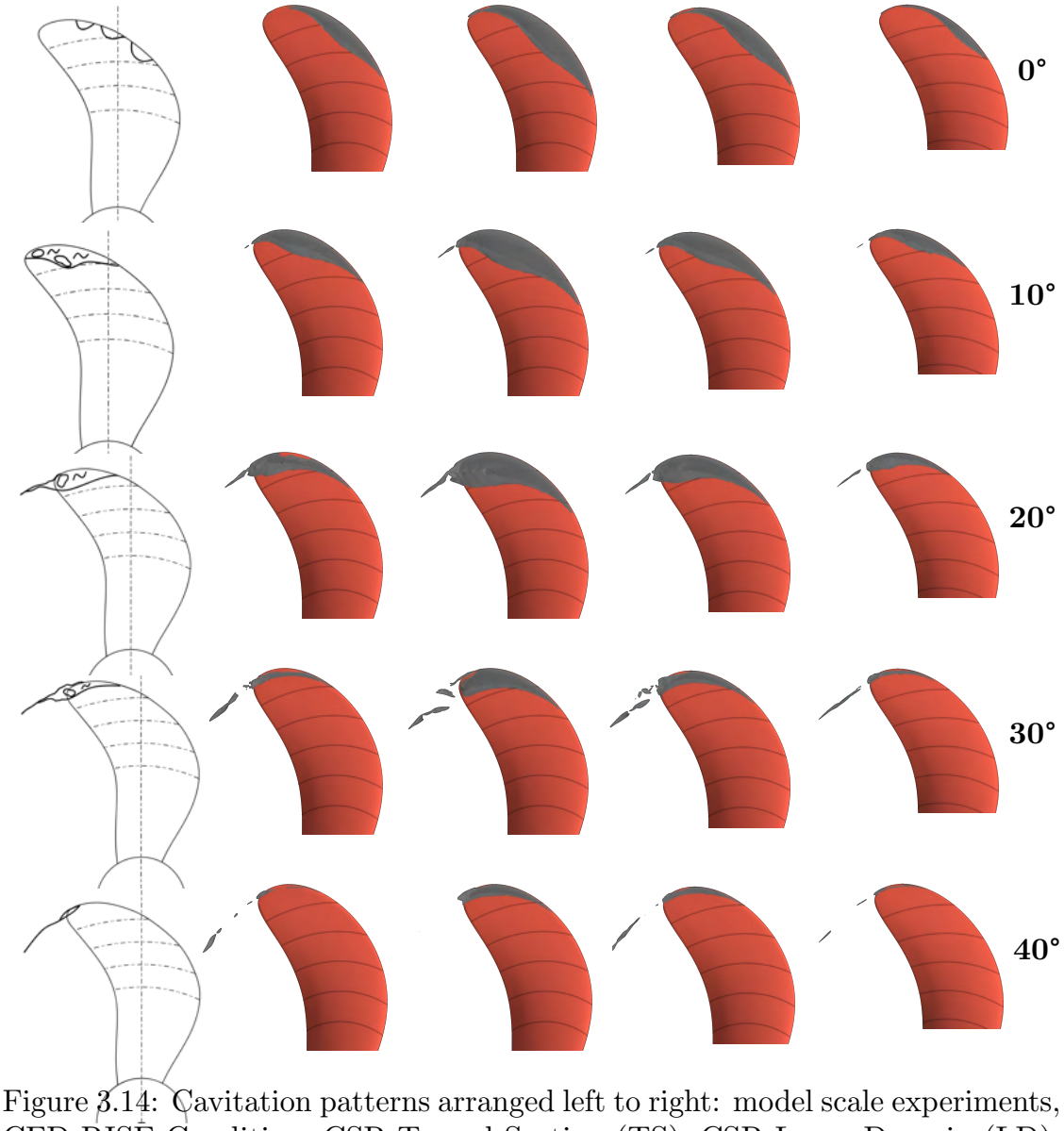

Figure 3.14: Cavitation patterns arranged left to right: model scale experiments, CFD RISE Condition, CSR Tunnel Section (TS), CSR Large Domain (LD), and CSR Full Scale.

Comparison for the pressure pulse levels between experiments and numerical predictions are presented in Figure 3.15 for a transducer D which is positioned above the propller as shown in Figure 3.9 (right). The 1st-order pressure pulse level is underpredicted by numerical results relative to the experiments. This is associated with the stable wakefield predicted by the RANS approach, which affects the intensity of the cavitation collapse. The highest levels recorded for the CSR condition are at the TS condition, followed by the LD and full scale conditions, which reflect the influence of blockage and scale effects. For the LD and full scale condition, pressure pulse levels decreased by approximate 15% and 32% relative to the TS condition.

While numerical simulations underpredict the 1st-order pressure pulse levels, they overpredict the higher-order components compared to experiments. The intermittent cavitation observed in the experiments, particularly for the tip vortex, will reduce the overall levels. This leads to larger discrepancies between numerical predictions and experimental measurements for these higher-order components. For the CSR condition, blockage and scale effects remain significant, consistent with the trends observed earlier.

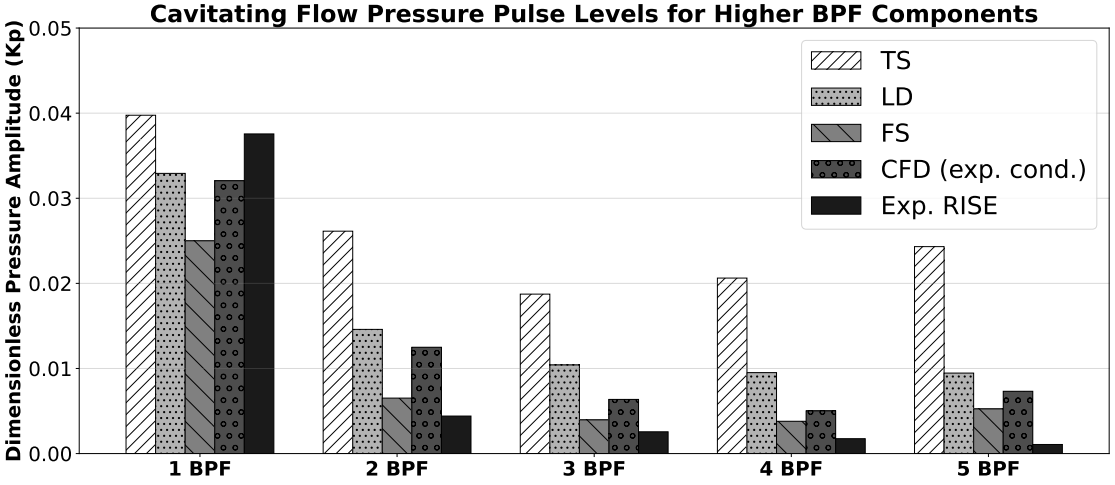

Figure 3.15: Pressure pulse levels of the first five BPF components at transducer D.

3.3 Cavitation Underwater Radiated Noise Methodology Applied to a Propeller Operating in-behind Condition

General Description

This study is a continuation of the previous investigation on scale effects for a propeller operating in-behind a hull. However, the conditions differ due to the operation of sea trial measurements. The sea trial measurements for underwater radiated noise were conducted by the Swedish Environmental Research Institute [55]. A total of eight hydrophones were deployed at various depths and ranges, and data was collected as the ship passed by. Additionally, near-field pressure pulse measurements were carried out using two transducers mounted on the aft by Kongsberg Maritime, as shown in Figure 3.16. Model scale experiments conducted by RISE follow the same procedure described in the previous section.

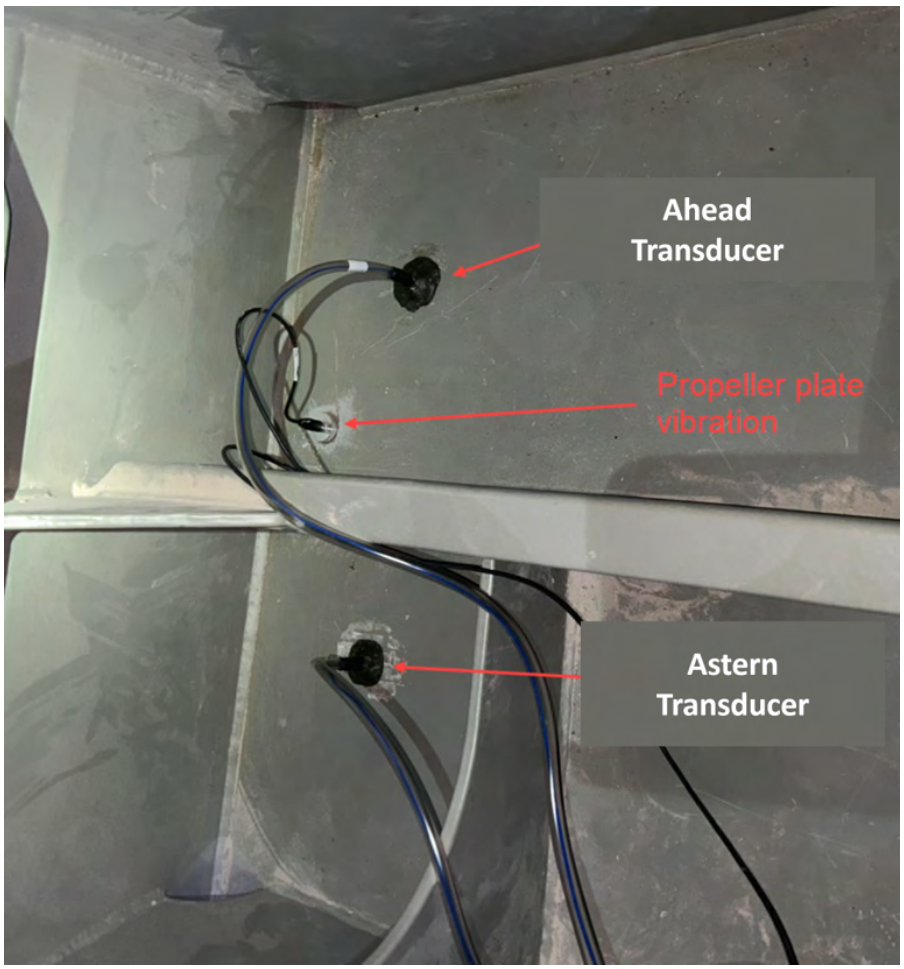

Figure 3.16: Two pressure transducers mounted on the aft and above the propeller during sea trials.

Results

Before discussing results on URN predictions, near field pressure pulse levels are presented in Figure 3.17. Good agreement between the measurements and numerical predictions is obtained for the 1st-order BPF levels, and relative differences are within 6%. For the model scale condition, the numerical results overpredict the levels relative to the model tests, while better agreement between the sea trials and full scale predictions. More variations in the levels are observed for higher-order BPF levels between model tests and predictions, as the experiments show much lower levels. This is attributed to the intermittent cavitation behavior observed during the tests. On the other hand, better agreement is obtained between predictions and sea trials for all higher-order components, though there is a slight underprediction from the numerical results. Nevertheless, the results are encouraging as the numerical predictions at full scale are in good agreement with the measured data.

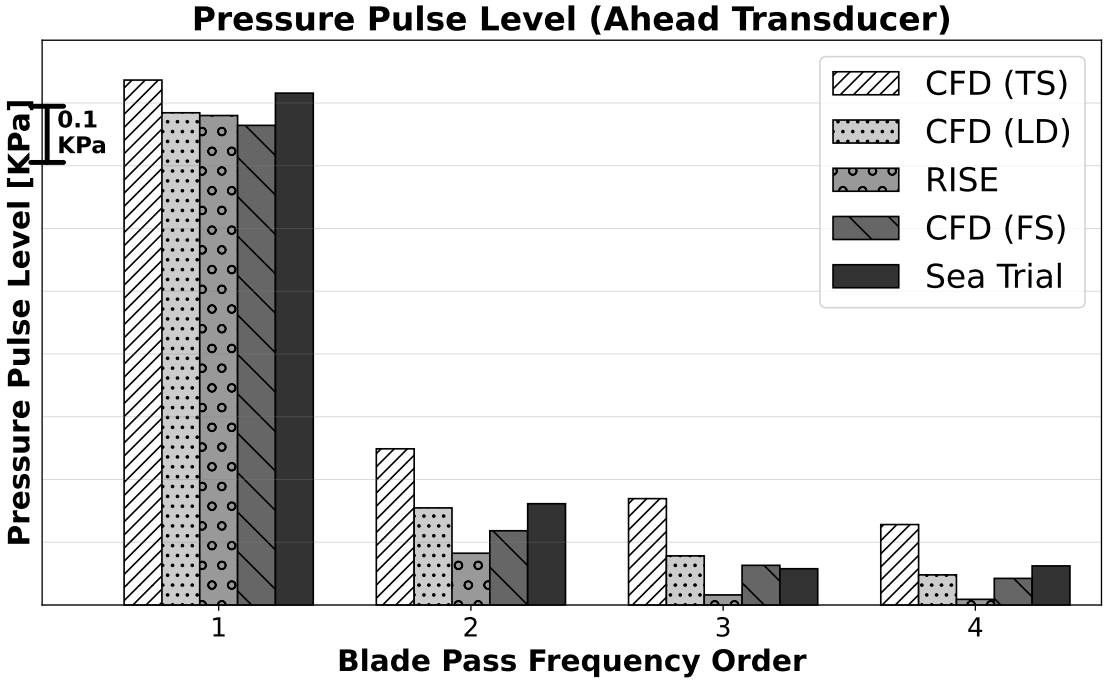

Figure 3.17: Pressure pulse levels from sea trials, model scale measurements, and numerical predictions.

Numerical predictions of underwater radiated noise are obtained using two approaches. The first approach uses the Ffowcs Williams–Hawkings (FW-H) acoustic analogy described in Section 2.2. Permeable Data Surfaces (PDS) are required to collect flow field information to use as an input for the acoustic analogy. To evaluate the influence of PDS size on the noise predictions, three spherical surfaces of different sizes are designed, as shown in Figure 3.18. The size of each surface is defined relative to the propeller radius R. In addition, the influence of receiver placement is investigated by using 410 receivers distributed across various positions on the propeller plane, as well as upstream and downstream of it.

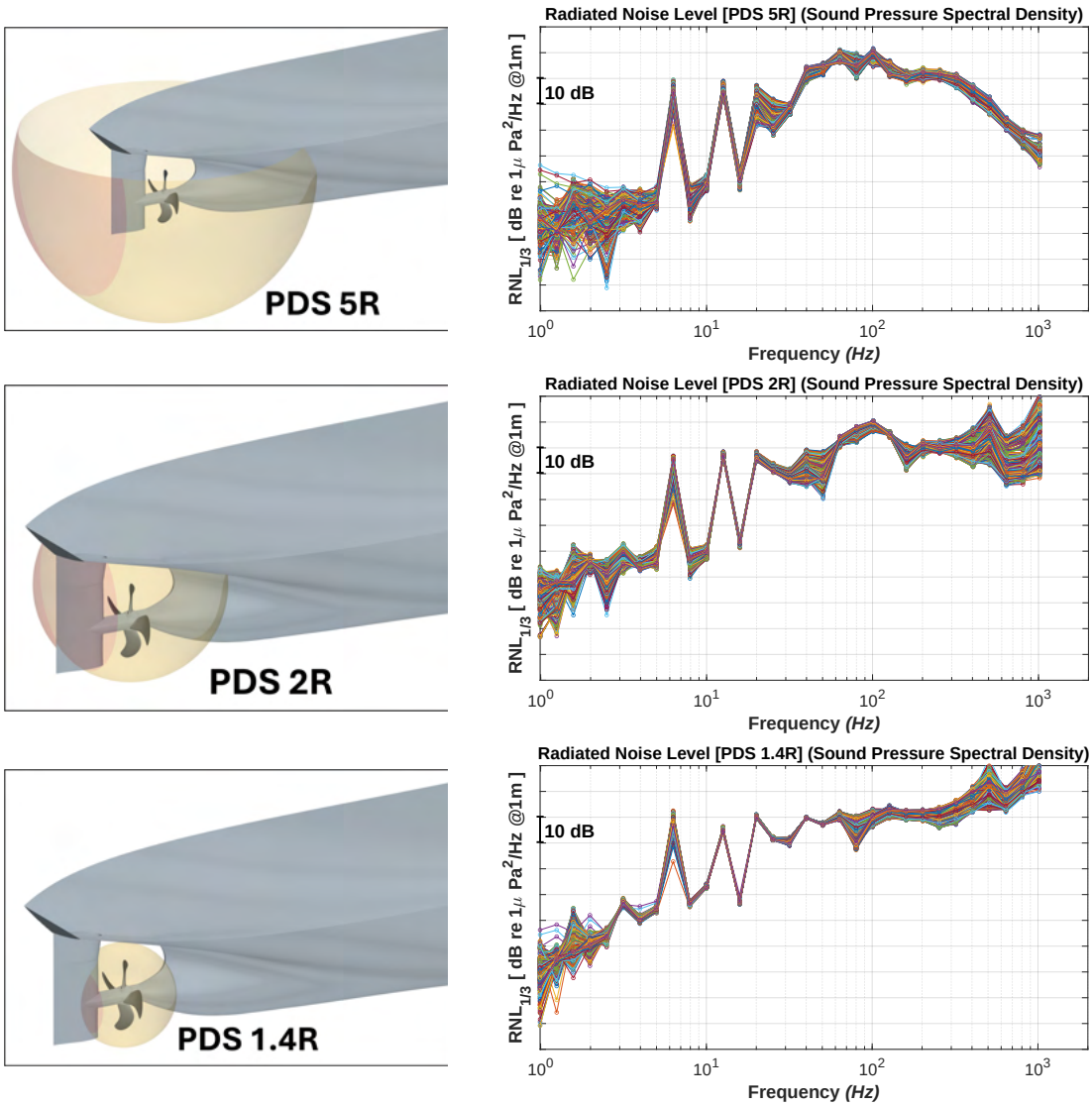

Figure 3.18: Designed Permeable Data Surfaces (Left) and their corresponding RNL computed for all 410 receivers.

The levels computed from PDS $5R$ show a typical noise spectrum that is expected for a cavitating propeller. The first two tonal peaks at frequencies 6.3 Hz and 12.6 Hz correspond to the first and second BPF levels. These tonal peaks are primarily dominated by the sheet cavitation noise, with a small contribution from the displaced fluid. In addition, two humps appear at approximately 70 Hz and 100 Hz which are associated with tip vortex cavitation, followed by a drop in levels for the high-frequency broadband spectrum. There is also a dependency on the receiver placement for the obtained noise level. Across all frequency levels, there is a significant variation/spread in the Radiated Noise Level (RNL) for all receivers. For instance, the RNL varies by approximately 19 dB for the first tonal peak which highlights a significant spread.

RNL predictions from the smaller surfaces $2R$ and $1.4R$ show that it is influenced by high-frequency sources above 100 Hz. To investigate and identify the source of this high-frequency content, Figure 3.19 (left) shows the spectral

el (dB/Hz)

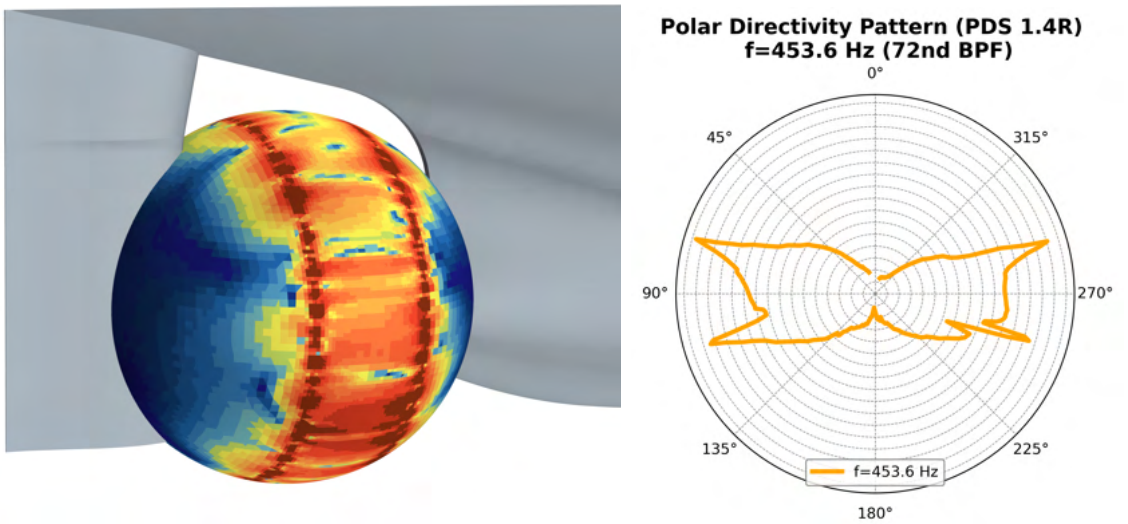

Figure 3.19: Directivity patterns at 453Hz (left) and polar directivity for PDS 1.4R (right)

density on the smallest PDS at the 72nd BPF, and the corresponding polar directivity on a single radial path (right). Separate and sharp parallel lines with much higher noise levels are observed on the surface which align with the sharp corners of the interface connecting the rotating and stationary regions. This shows that the high frequency noise contaminating the broadband spectrum for the smaller data surfaces originates from the numerical noise introduced by the interface. As a result, unrealistically high noise levels appear in the broadband predictions.

The second approach for noise prediction models cavitation as a monopole noise source, as described in Section 2.3. The total vapor volume is collected during the simulation over five propeller revolutions. Equation 2.23 is then applied to compute the acoustic pressure signal based on the second-order derivative of the vapor volume. However, the numerical differentiation introduces spurious high frequency content which contaminates the signal. To address this, a modified version of the Locally Weighted Scatterplot Smoothing (LOWESS) method [56] is applied to the vapor volume data. The smoothed volume curve is shown in black in Figure 3.20, capturing the general behavior of the original signal with minimal deviation.

Furthermore, Figure 3.20 (bottom) compares the RNL obtained with and without the LOWESS smoothing applied to the cavitation volume signal. The smoothed signal is similar to the original below 100 Hz. However, the broadband levels in the original signal are contaminated with the spurious noise from the numerical differentiation which leads to the unphysical increase in levels. This high frequency noise is successfully filtered with the LOWESS smoothing which results in a more physically representative noise spectrum. We refer to this approach as the Hybrid Analytical-Numerical (A-N) method.

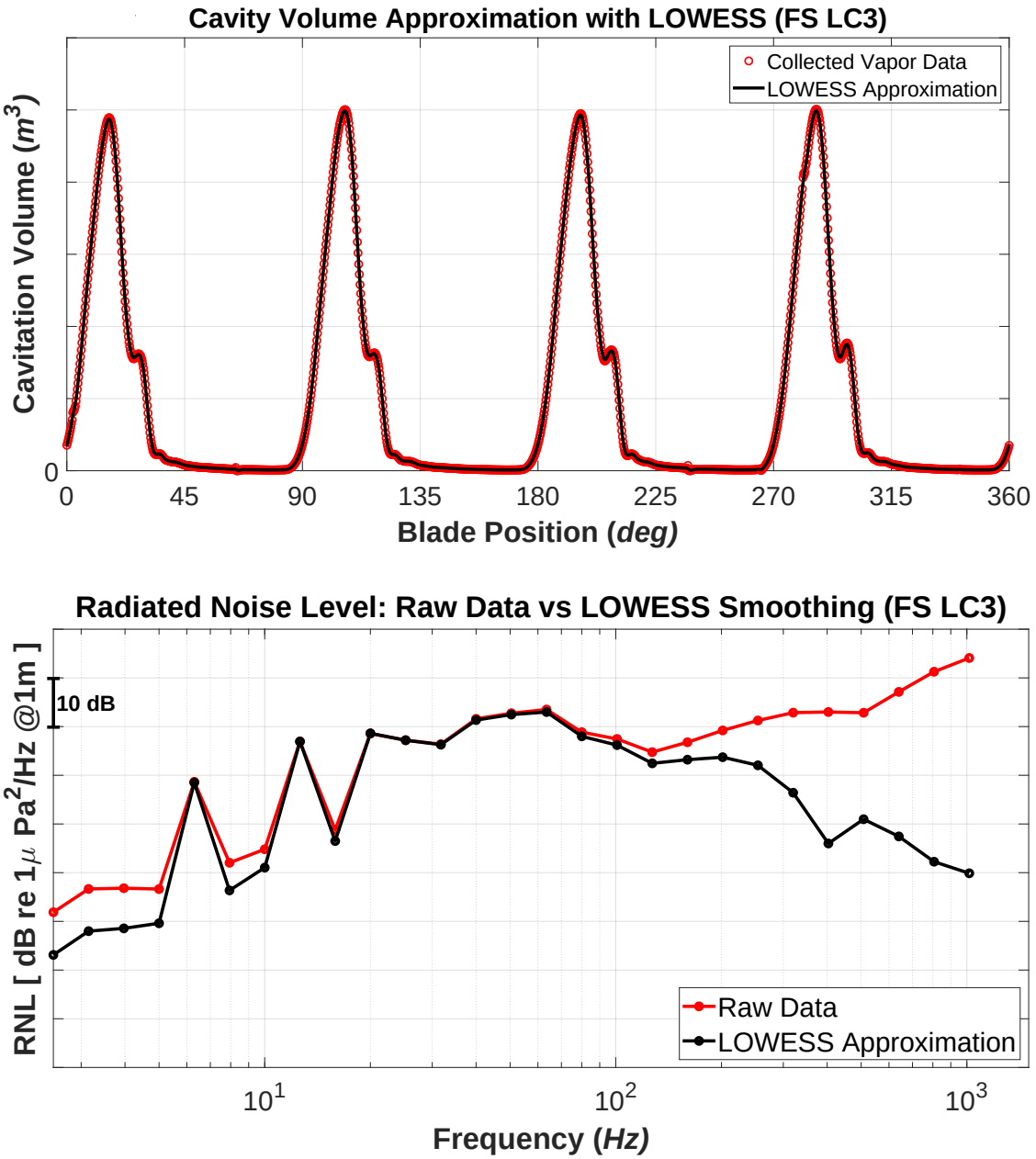

Figure 3.20: Analysis of FS LC3 condition: Top shows LOESS smoothing results, bottom displays spectral density levels

Results from the sea trial measurements and model scale tests are presented in Figure 3.21, together with full scale numerical predictions from FW-H acoustic analogy and the analytical-numerical method. During the sea trials, cavitation was not prominent, and low-frequency noise is dominated by the engine. The noise levels are much higher than what is obtained by the model test and numerical predictions at the lower frequency range. For the model scale test, the tonal components align with the blade passing frequencies and are mainly attributed to sheet cavitation noise. Broadband humps are also observed at 100 Hz, 500 Hz, and 700 Hz, which are associated with the tip vortex and the collapse of other small cavities.

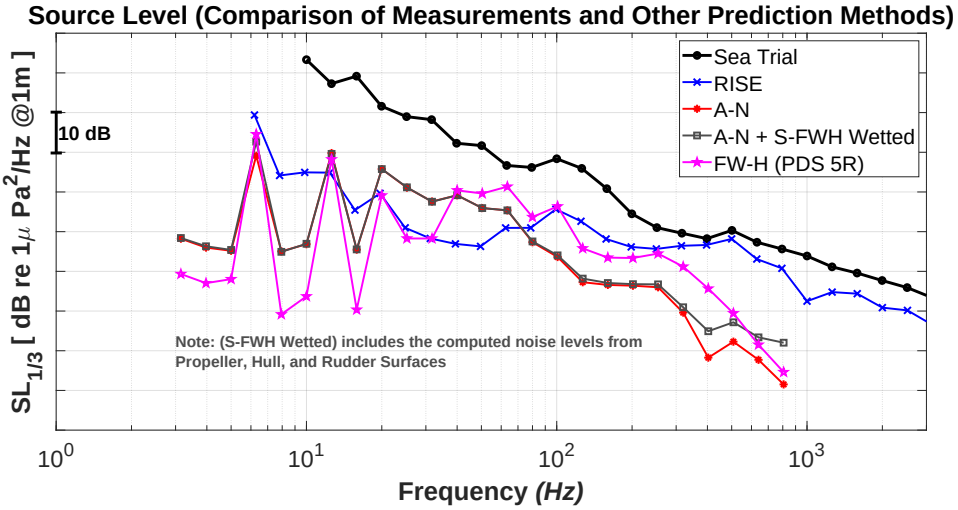

Figure 3.21: Narrowband source noise levels from sea trials, model scale tests, and cavitation noise from the hybrid Analytical-Numerical (A-N) approach (at full scale condition)

Predictions obtained by the FW-H and A-N methods provide similar results for the tonal components, but larger discrepancies for the higher frequencies. The FW-H provides closer levels with the measurements, particularly at the 100 Hz hump. This leads to the conclusion that there are sources in the broadband spectrum that are not captured with the A-N approach, which is not from neglecting wetted flow noise as indicated by the grey line in Figure 3.21.

Further investigation through the decomposition of the monopole and dipole terms captured by acoustic analogy indicate that broadband levels are influenced by dipole sources. The thickness/monopole term from the FW-H acoustic analogy shown in Figure 3.22 drop in the broadband levels similar to the the A-N approach, while the levels beyond 80 Hz are primarily from the loading term (dipole contributions). The sources of these contributions are mainly from the Aft, indicating hull scattering is important to consider.

Figure 3.23 shows the Source Level predictions for both model and full scale cases using the A-N approach in combination with the S-FWH from the hull aft surface. When including scattering effects from the hull surface, the broadband source level predictions significantly improved relative to the measured levels. The model scale TS condition now shows good agreement with RISE measurements for the hump at 100 Hz. However, there is still large

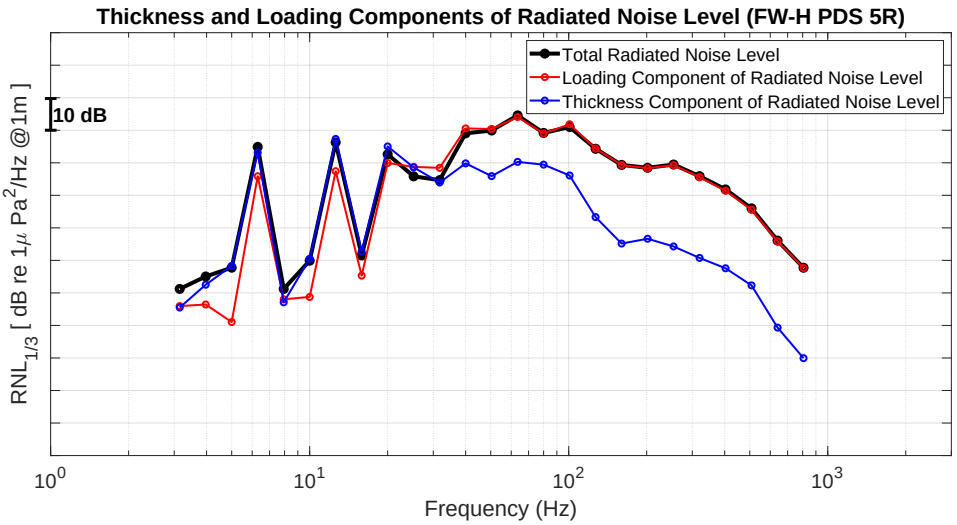

Figure 3.22: Decomposition of the Thickness (monopole) and Loading (dipole) terms as computed from the permeable data surface 5R.

discrepancies in broadband levels beyond 200 Hz. The higher levels obtained from the tests are due to the stronger tip vortex dynamics and more violent bursting, which will be underpredicted with the RANS approach. Finally, predictions with the Large Domain (LD) case lead to lower levels across all frequencies due to the changes in wakefield, cavitation volume, and its dynamics.

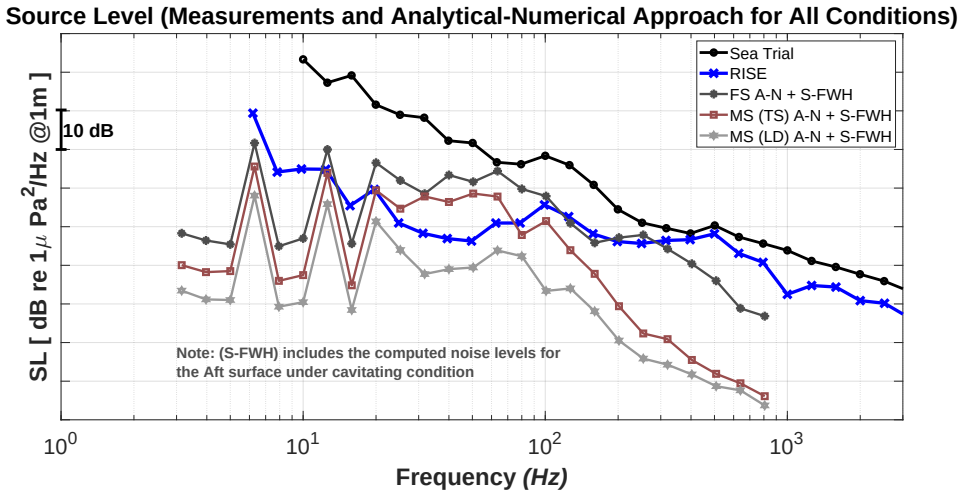

Figure 3.23: Source Noise Level from experimental measurement, model tests, and the hybrid A-N method for all conditions.

In summary, the hybrid analytical-numerical approach is developed for cases where cavitation is the dominant noise source, and results highlight the challenges in obtaining reliable URN predictions. A large variation in noise levels between model and full scale measurement campaigns is observed, though some of these differences are understood. While, hybrid analytical-numerical approach shows good correlation with measured data up to $200Hz$, significant variations remain in the broadband levels.

Chapter 4

Summary and Suggestions for Future Work

This thesis investigates scale effects on cavitation and underwater radiated noise using two test cases: a cavitating hydrofoil and a propeller operating in a wakefield.

In the case of the hydrofoil, the analysis focuses on scale effects on cavitation and cloud shedding. At higher Reynolds number, the attached cavity extends longer but detaches slightly earlier. While the evolution of the cloud and larger scale structure remain similar, smaller-scale structures are more pronounced at higher Reynolds numbers due to the broader energy spectrum.

In the case of the propeller operating in-behind, scale effects are more pronounced due to the interaction with the wakefield. At the higher Reynolds number, the wakefield is thinner, resulting in a more lightly loaded blade at the wake peak. This leads to less cavitation development at full scale when compared with model scale predictions. As a result, variations in the predicted pressure pulses and noise levels were obtained. In addition, the influence of blockage is studied and results show that cavitation tunnel size influences wakefield and cavitation dynamics. Finally, an alternative prediction methodology for underwater radiated noise from cavitation is proposed. Discrepancies were found in the predicted levels when compared with the measurements, though some of those variations are understood.

Proposed future work will mainly focus on underwater radiated noise. It would be of interest to apply the alternative prediction method on other cases where cavitation is more prominent for further verification. In addition, the results demonstrate limitations in obtaining reliable broadband noise levels with the RANS approach. Therefore, it would be interesting to investigate higher fidelity models, such as Detached Eddy simulations. It is expected that a more dynamic wake field upstream of the propeller will be predicted, which will influence cavitation dynamics. In addition, since RANS is known to underpredict tip vortex structures, higher fidelity models are expected to improve the prediction of the tip vortex and broadband levels. Further investigations on noise mitigation techniques will be one key area of this

research. The goal is to apply existing noise prediction methods to reduce the noise signature of vessels. More specifically, techniques aiming at mitigation of the sheet and tip vortex dynamics will be explored. The overall objective is to provide recommendations that enable the design of more silent vessels.

Bibliography

[1] B. C. Suedel, A. D. McQueen, J. L. Wilkens and M. P. Fields, "Evaluating effects of dredging-induced underwater sound on aquatic species: A literature review," 2019.

[2] M. Andersson, R. Bensow, D. Glebe, I.-M. Hassellöv, E. Lalander, D. Langlet, K. Larsson, L.-G. Malmberg, E.-L. Sundblad and M. Svedendahl, "Management measures to reduce continuous underwater noise from shipping," Swedish Institute for the Marine Environment, Report 2023:3, 2023.

[3] G. V. Frisk, "Noiseonomics: The relationship between ambient noise levels in the sea and global economic trends," *Scientific reports*, vol. 2, no. 1, p. 437, 2012.

[4] J.-P. Jalkanen, L. Johansson, M. H. Andersson, E. Majamäki and P. Sigray, "Underwater noise emissions from ships during 2014–2020," *Environmental Pollution*, vol. 311, p. 119 766, 2022.

[5] L. Bedriñana-Romano, R. Hucke-Gaete, F. A. Viddi, D. Johnson, A. N. Zerbini, J. Morales, B. Mate and D. M. Palacios, "Defining priority areas for blue whale conservation and investigating overlap with vessel traffic in chilean patagonia, using a fast-fitting movement model," *Scientific reports*, vol. 11, no. 1, p. 2709, 2021.

[6] C. M. Duarte, L. Chapuis, S. P. Collin, D. P. Costa, R. P. Devassy, V. M. Eguiluz, C. Erbe, T. A. Gordon, B. S. Halpern, H. R. Harding *et al.*, "The soundscape of the anthropocene ocean," *Science*, vol. 371, no. 6529, eaba4658, 2021.

[7] International Maritime Organization, *Guidelines for the reduction of underwater noise from commercial shipping to address adverse impacts on marine life*, 2014.

[8] International Maritime Organization, *Revised guidelines for the reduction of underwater radiated noise from shipping to address adverse impacts on marine life*, 2023.

[9] R. J. Urick, "Principles of underwater sound-2," 1975.

[10] K. Abrahamsen, "The ship as an underwater noise source," in *Proceedings of Meetings on Acoustics*, AIP Publishing, vol. 17, 2012.

[11] M. Billet and J. Holl, "Scale effects on various types of limited cavitation," 1981.

[12] L. Larsson and H. C. Raven, *Ship Resistance and Flow* (The Principles of Naval Architecture Series), J. R. Paulling, Ed. Society of Naval Architects and Marine Engineers, 2010.

[13] J. Szantyr, "Scale effects in cavitation experiments with marine propeller models," *Polish Maritime Research*, vol. 13, pp. 3–10, 2006.

[14] E. Amromin, "Analysis of viscous effects on cavitation," 2000.

[15] P. B. Regener, Y. Mirsadraee and P. Andersen, "Nominal vs. effective wake fields and their influence on propeller cavitation performance," *Journal of Marine Science and Engineering*, vol. 6, no. 2, p. 34, 2018.

[16] G Kuiper, "Cavitation scale effects: A case study," *International Shipbuilding Progress*, vol. 25, no. 284, pp. 81–90, 1978.

[17] M. E. Duttweiler and C. E. Brennen, "Surge instability on a cavitating propeller," *Journal of Fluid Mechanics*, vol. 458, pp. 133–152, 2002.

[18] ITTC 7.5-04-04-01, *Underwater noise from ships: Full scale measurements*, 2024. [Online]. Available: `https://www.ittc.info/media/11982/75-04-04-01.pdf`.

[19] A. P. Keller, "Cavitation scale effects-empirically found relations and the correlation of cavitation number and hydrodynamic coefficients," *http://resolver. caltech. edu/cav2001: lecture. 001*, 2001.

[20] S. Mukherjee and H. Gomez, "Effect of dissolved gas on the tensile strength of water," *Physics of Fluids*, vol. 34, no. 12, 2022.

[21] Z. Gao, W. Wu and B. Wang, "The effects of nanoscale nuclei on cavitation," *Journal of Fluid Mechanics*, vol. 911, A20, 2021.

[22] G. Tani, B. Aktas, M. Viviani and M. Atlar, "Two medium size cavitation tunnel hydro-acoustic benchmark experiment comparisons as part of a round robin test campaign," *Ocean Engineering*, vol. 138, pp. 179–207, 2017.

[23] G. Tani, M. Viviani, M. Felli, F. H. Lafeber, T. Lloyd, B. Aktas, M. Atlar, S. Turkmen, H. Seol, J. Hallander and N. Sakamoto, "Noise measurements of a cavitating propeller in different facilities: Results of the round robin test programme," *Ocean Engineering*, vol. 213, p. 107 599, 2020, ISSN: 0029-8018. DOI: `10.1016/j.oceaneng.2020.107599`.

[24] Q. Yang, Y. Wang and Z. Zhang, "Scale effects on propeller cavitating hydrodynamic and hydroacoustic performances with non-uniform inflow," *Chinese Journal of Mechanical Engineering*, vol. 26, no. 2, pp. 414–426, 2013.

[25] A. Soydan and S. Bal, "An investigation of scale effects on marine propeller under cavitating and non-cavitating conditions," *Ship Technology Research*, vol. 68, no. 3, pp. 166–178, 2021.

[26] B. Ji, X.-W. Luo, Y.-L. Wu, S.-H. Liu, H.-Y. Xu and A. Oshima, "Numerical investigation of unsteady cavitating turbulent flow around a full scale marine propeller," *Journal of hydrodynamics, ser. B*, vol. 22, no. 5, pp. 747–752, 2010.

[27] V. Viitanen, T. Siikonen and A. Sánchez-Caja, "Cavitation on model-and full-scale marine propellers: Steady and transient viscous flow simulations at different reynolds numbers," *Journal of Marine Science and Engineering*, vol. 8, no. 2, p. 141, 2020.

[28] D. Ponkratov, "DES prediction of cavitation erosion and its validation for a ship scale propeller," in *Journal of Physics: Conference Series*, IOP Publishing, vol. 656, 2015, p. 012 055.

[29] D.-Q. Li, J. Hallander and T. Johansson, "Predicting underwater radiated noise of a full scale ship with model testing and numerical methods," *Ocean Engineering*, vol. 161, pp. 121–135, 2018.

[30] G. Bark, "Prediction of propeller cavitation noise from model tests and its comparison with full scale data," *Journal of Fluids Engineering*, vol. 107, no. 1, pp. 112–119, 1985. DOI: 10.1115/1.3242424.

[31] F. H. Lafeber, T. Lloyd and J. Bosschers, "Validation of underwater radiated noise predictions for a merchant vessel using full-scale measurements," in *INTER-NOISE and NOISE-CON Congress and Conference Proceedings*, Institute of Noise Control Engineering, vol. 255, 2017, pp. 3857–3866.

[32] B. Aktas, M. Atlar, S. Turkmen, W. Shi, R. Sampson, E. Korkut and P. Fitzsimmons, "Propeller cavitation noise investigations of a research vessel using medium size cavitation tunnel tests and full-scale trials," *Ocean engineering*, vol. 120, pp. 122–135, 2016.

[33] G. Tani, M. Viviani, M. Ferrando and E. Armelloni, "Aspects of the measurement of the acoustic transfer function in a cavitation tunnel," *Applied Ocean Research*, vol. 87, pp. 264–278, 2019.

[34] J. E. Ffowcs Williams and D. L. Hawkings, "Sound generation by turbulence and surfaces in arbitrary motion," *Philosophical Transactions of the Royal Society of London. Series A, Mathematical and Physical Sciences*, vol. 264, no. 1151, pp. 321–342, 1969.

[35] A. K. Lidtke, T. Lloyd, F. H. Lafeber and J. Bosschers, "Predicting cavitating propeller noise in off-design conditions using scale-resolving CFD simulations," *Ocean Engineering*, vol. 254, p. 111 176, 2022.

[36] S. Sezen and M. Atlar, "Marine propeller underwater radiated noise prediction with the fwh acoustic analogy part 2: Assessment of model scale propeller hydroacoustic performance under non-uniform flow conditions," *Ocean Engineering*, vol. 270, p. 113 443, 2023.

[37] J. Kimmerl and M. Abdel-Maksoud, "Visualization of underwater radiated noise in the near-and far-field of a propeller-hull configuration using cfd simulation results," *Journal of marine science and engineering*, vol. 11, no. 4, p. 834, 2023.

[38] C Testa, F Porcacchia, S Zaghi and M Gennaretti, "Study of a FWH-based permeable-surface formulation for propeller hydroacoustics," *Ocean Engineering*, vol. 240, p. 109 828, 2021.

[39] Z. Nitzkorski and K. Mahesh, "A dynamic end cap technique for sound computation using the ffowcs williams and hawkings equations," *Physics of Fluids*, vol. 26, no. 11, 2014.

[40] S. Ahmed, "On the noise generated by a ship propeller," Ph.D. dissertation, UNSW Sydney, 2020.

[41] M. Ge, U. Svennberg and R. E. Bensow, "Investigations on prediction of ship noise using the FWH acoustic analogy with incompressible flow input," *Ocean Engineering*, vol. 257, p. 111 531, 2022.

[42] M. Vikström, U. Svennberg, M. Ge and R. E. Bensow, "The effect of porous data surface shape and size on ship noise prediction using the FWH acoustic analogy with incompressible solver for a cavitating propellers," in *Proceedings of the 7th International Symposium of Marine Propulsors*, 2022.

[43] F. R. Menter, M. Kuntz, R. Langtry *et al.*, "Ten years of industrial experience with the SST turbulence model," *Turbulence, heat and mass transfer*, vol. 4, no. 1, pp. 625–632, 2003.

[44] G. H. Schnerr and J. Sauer, "Physical and numerical modeling of unsteady cavitation dynamics," in *Fourth international conference on multiphase flow*, ICMF New Orleans New Orleans, LO, USA, vol. 1, 2001, pp. 1–12.

[45] J.-L. Reboud, B. Stutz and O. Coutier, "Two phase flow structure of cavitation: Experiment and modeling of unsteady effects," in *3rd international symposium on cavitation CAV1998, Grenoble, France*, vol. 26, 1998, pp. 1–8.

[46] O. Coutier-Delgosha, R Fortes-Patella and J.-L. Reboud, "Evaluation of the turbulence model influence on the numerical simulations of unsteady cavitation," *J. Fluids Eng.*, vol. 125, no. 1, pp. 38–45, 2003.

[47] R. E. Bensow, "Simulation of the unsteady cavitation on the Delft Twist11 foil using RANS, DES and LES," in *Second international symposium on marine propulsors*, 2011.

[48] M. J. Lighthill, "On sound generated aerodynamically i. general theory," *Proceedings of the Royal Society of London. Series A. Mathematical and Physical Sciences*, vol. 211, no. 1107, pp. 564–587, 1952.

[49] M. J. Lighthill, "On sound generated aerodynamically ii. turbulence as a source of sound," *Proceedings of the Royal Society of London. Series A. Mathematical and Physical Sciences*, vol. 222, no. 1148, pp. 1–32, 1954.

[50] N. Curle, "The influence of solid boundaries upon aerodynamic sound," *Proceedings of the Royal Society of London. Series A. Mathematical and Physical Sciences*, vol. 231, no. 1187, pp. 505–514, 1955.

[51] K William, *Mechanics of Flow-induced Sound and Vibration, Volume 1-General Concepts*. Elsevier Science Publishing Company, 2017.

[52] S Ianniello, R Muscari and A Di Mascio, "Ship underwater noise assessment by the acoustic analogy. part i: Nonlinear analysis of a marine propeller in a uniform flow," *Journal of marine Science and technology*, vol. 18, pp. 547–570, 2013.

[53] S. Ianniello and E. De Bernardis, "Farassat's formulations in marine propeller hydroacoustics," *International Journal of Aeroacoustics*, vol. 14, no. 1-2, pp. 87–103, 2015.

[54] E.-J. Foeth, "The structure of three-dimensional sheet cavitation," 2008.

[55] C. Andersson, M. Linné, T. Johansson and M. Andersson, "Measuring ship underwater radiated noise in shallow waters - why not in the near field?" In *Proceedings of the Institute of Acoustics - ICUA2024*, vol. 46, Bath, UK: Institute of Acoustics, 2024. DOI: 10.25144/22211.

[56] W. S. Cleveland, "Robust locally weighted regression and smoothing scatterplots," *Journal of the American statistical association*, vol. 74, no. 368, pp. 829–836, 1979.